

Multi-slice CT Technology

THOMAS FLOHR and BERND OHNESORGE

CONTENTS

3.1	Evolution from 1 to 64 Slices	41
3.2	Principles of Multi-slice CT System Design	45
3.3	Multi-slice CT Acquisition and Reconstruction for Body Imaging	52
3.3.1	Definition of the Pitch	52
3.3.2	The Cone-Angle Problem in Multi-slice CT	53
3.3.3	Multi-slice Spiral Reconstruction Neglecting the Cone-Beam Geometry	54
3.3.3.1	180° and 360° Multi-slice Linear Interpolation	54
3.3.3.2	z-Filter Approaches	56
3.3.4	Multi-slice Spiral Reconstruction with Cone-Beam Algorithms	58
3.3.4.1	Overview of Cone-Beam Reconstruction Algorithms	58
3.3.4.2	3D Filtered Back-Projection	58
3.3.4.3	Adaptive Multiple Plane Reconstruction	59
3.3.4.4	Weighted Hyperplane Reconstruction	61
3.3.4.5	Double z-Sampling	62
	References	67

3.1

Evolution from 1 to 64 Slices

Computed tomography (CT) was introduced in the early 1970s and has revolutionized not only diagnostic radiology, but also the entire practice of medicine. In the early 1990s, the introduction of spiral CT constituted a further evolutionary step in the development and ongoing refinement of CT imaging techniques (KALENDER 1990, CRAWFORD 1990). Until then, the examination volume had to be covered by subsequent axial scans in a «step-

and-shoot» mode, the so-called sequence-scan technique. Consequently, axial scanning required long examination times because of the inter-scan delays necessary to move the table incrementally from one scan position to the next, and it was prone to misregistration of anatomical details due to the potential movement of relevant anatomical structures between two scans, e. g., by patient motion, breathing, or swallowing. With spiral CT, the patient table is continuously translated while scan data are acquired. The prerequisite for the success of spiral scanning was the introduction of slip-ring gantries, which eliminated the need to rewind the gantry after each rotation and enabled continuous data acquisition during multiple rotations. For the first time, volume data could be acquired without the danger of misregistration or double-registration of anatomical details. Images could be reconstructed at any position along the patient axis (longitudinal axis), and overlapping image reconstruction could be used to improve longitudinal resolution. Volume data became the very basis for applications such as CT angiography (RUBIN 1995), which has revolutionized non-invasive assessment of vascular disease. The ability to acquire volume data also paved the way for the development of 3D image-processing techniques, such as multi-planar reformations (MPR), maximum intensity projections (MIP), surface-shaded displays (SSD), and volume-rendering techniques (VRT) (NAPEL 1993). These have become vital components of medical imaging today.

Ideally, volume data are of high spatial resolution and isotropic in nature, i.e., the data element («voxel») of each image is of equal dimensions in all three spatial axes, and forms the basis for image display in arbitrarily oriented imaging planes. For most clinical scenarios, however, single-slice spiral

CT with 1-s gantry rotation time is unable to fulfill these prerequisites. To avoid motion artifacts and to optimally use the contrast bolus, spiral CT body examinations need to be completed within a certain timeframe of, ordinarily, one patient breath-hold (25–30 s). If a large scan range, such as the entire thorax or abdomen (30 cm), has to be covered with single-slice spiral CT within a single breath-hold, a thick collimation of 5–8 mm must be used. While the in-plane resolution of a CT image depends on the system geometry and on the reconstruction kernel selected by the user, the longitudinal (z-) resolution is determined by the collimated slice width and the spiral interpolation algorithm. A thick collimation of 5–8 mm results in a considerable mismatch between the longitudinal resolution and the in-plane resolution, which is usually 0.5–0.7 mm depending on the reconstruction kernel. Thus, with single-slice spiral CT, the ideal of isotropic resolution can only be achieved for very limited scan ranges (KALENDER 1995).

Strategies to achieve more substantial volume coverage with improved longitudinal resolution have included the simultaneous acquisition of more than one slice at a time and a reduction of the gantry rotation time. Interestingly, the very first medical CT scanners were 2-slice systems, such as the EMI head scanner, introduced in 1972, or the Siemens SIRETOM, introduced in 1974. With the advent of whole-body fan-beam CT systems for general radiology, 2-slice acquisition was no longer used. Apart from a dedicated 2-slice system for cardiac applications, the IMATRON C-100, introduced in 1984, the first step towards multi-slice acquisition in general radiology was a 2-slice CT scanner introduced in 1993 (Elscent TWIN) (LIANG 1996). In 1998, all major CT manufacturers introduced multi-slice CT (MSCT) systems, which typically offered simultaneous acquisition of 4 slices at a rotation time of down to 0.5 s. This was a considerable improvement in scan speed and longitudinal resolution and offered better utilization of the available X-ray power (KLINGENBECK 1999, MCCOLLOUGH 1999, OHNESORGE 1999, HU 2000). These developments were quickly recognized as revolutionary improvements that would eventually enable users to do real isotropic 3D imaging. Consequently, all vendors pushed towards more and more slices, turning the number of slices into

the most important performance characteristic of a CT scanner. Figure 3.1 shows the performance of new CT systems, measured by the number of slices per rotation, at the time of their market introduction. Interestingly, analogous to “Moore’s Law” in the computer industry, the increase in the number of slices has been exponential, approximately doubling every 18 months.

Simultaneous acquisition of N slices results in an N -fold increase in speed if all other parameters, such as slice thickness, are unchanged. This increased performance of multi-slice CT compared to single-slice CT allowed for the optimization of a variety of clinical protocols. The examination time for standard protocols could be significantly reduced, which proved to be of immediate clinical benefit for the quick and comprehensive assessment of trauma victims and non-cooperative patients. Alternatively, the scan range that could be covered within a certain scan time was extended by a factor of N , which is relevant for oncological staging or for CT angiography with extended coverage, for example, of the lower extremities (RUBIN 2001). The most important clinical benefit, however, proved to be the ability to scan a given anatomic volume within a given scan time with substantially reduced slice width, at N -times-increased longitudinal resolution. This way, for many clinical applications, the goal of isotropic resolution was within reach with 4-slice CT systems. Examinations of the entire thorax (SCHOEPPF 2001) or

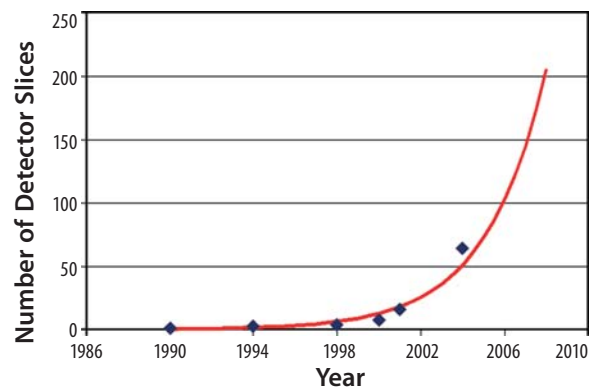


Fig. 3.1. The number of slices of new CT scanners at the time of market introduction. Performance in terms of slice number doubles about every 18 months

abdomen (KLINGENBECK 1999) could now routinely be performed with a collimated slice width of 1 mm or 1.25 mm. Multi-slice CT also expanded into areas previously considered beyond the scope of conventional spiral CT scanners, such as routine vascular diagnosis (OHNESORGE 2001, SCHOEPF 2003), high-resolution low dose CT of the lung (SWENSEN 2002), virtual CT colonography (MACARI 2002, WESSLING 2003), and cardiac imaging with the addition of ECG gating capability. The introduction of 4-slice CT with a gantry rotation time of 0.5 s and dedicated image-reconstruction approaches represented a breakthrough for mechanical CT in cardiac imaging. The temporal resolution for the acquisition of an image was improved to 250 ms and less (KACHELRIESS 2000, OHNESORGE 2000), sufficient for motion-free imaging of the heart in the mid- to end-diastolic phase at slow to moderate heart rates (HONG 2001). With four simultaneously acquired slices, coverage of the entire heart volume with thin slices and ECG-gating within a single breath-hold became feasible, enabling non-invasive visualization of the cardiac morphology and coronary arteries (OHNESORGE 2000, ACHENBACH 2000, KNEZ 2000, NIEMAN 2001).

Despite all these promising advances, clinical challenges and limitations remained for 4-slice CT systems. True isotropic resolution for routine applications had not yet been achieved, since a longitudinal resolution of about 1 mm does not fully match the in-plane resolution of about 0.5–0.7 mm in a routine scan of the chest or abdomen. For large volumes, such as CT angiography of lower-extremity run-off (RUBIN 2001), thicker (i.e. 2.5 mm) collimated slices had to be chosen to complete the scan within a reasonable timeframe. Scan times were often too long to allow image acquisition during pure arterial phase. For CT angiography of the circle of Willis, for instance, a scan range of about 100 mm must be covered (VILLABLANCA 2002). With 4-slice CT, at a collimated slice width of 1 mm, a pitch of 1.5, and 0.5 s gantry rotation time, this volume can be covered in a scan time of about 9 s, which is not fast enough to avoid venous overlay assuming a cerebral circulation time of less than 5 s. For ECG-gated coronary CT angiography, stents or severely calcified arteries constituted a diagnostic dilemma, mainly due to partial volume artifacts as a consequence of insufficient longitudinal resolution (NIEMAN 2001).

For patients with higher heart rates, careful selection of separate reconstruction intervals for different coronary arteries has been mandatory (KOPP 2001). The breath-hold time of about 40 s required to cover the entire heart volume (~12 cm) with 4-slice CT is almost impossible for patients with manifest heart disease to comply with.

As a next step, the introduction of an 8-slice CT system in 2000 enabled shorter scan times, but did not yet provide improved longitudinal resolution (thinnest collimation 8×1.25 mm). The latter was achieved with the introduction of 16-slice CT (FLOHR 2002a, FLOHR 2002b), which made it possible to routinely acquire substantial anatomic volumes with isotropic sub-millimeter spatial resolution. Improved longitudinal resolution goes hand in hand with the considerably reduced scan times that enable high-quality examinations in severely debilitated and severely dyspneic patients (Fig. 3.2). Clinical practice suggests the potential of 16-slice CT angiography to replace interventional catheter angiography in the evaluation of carotid artery stenosis (LELL 2002). For patients with suspicion of ischemic stroke, both the status of the vessels supplying the brain and the location of the intracranial occlusion can be assessed in the same examination (ERTL-WAGNER 2002). Additional brain-perfusion CT permits differentiation of irreversibly damaged brain tissue from reversibly impaired tissue at risk (TOMANDL 2003). Examining the entire thorax (350 mm) with sub-millimeter collimation requires a scan time of approximately 11 s. Due to the short breath-hold time, central and peripheral pulmonary embolism can be reliably and accurately diagnosed (REMY-JARDIN 2002, SCHOEPF 2003). Whole-body angiographic studies with sub-millimeter resolution in a single breath-hold are also possible with 16-slice CT. Compared to invasive angiography, the same morphological information is obtained (WINTERSPERGER 2002a, WINTERSPERGER 2002b). ECG-gated cardiac scanning with 16-slice CT systems benefits from both improved temporal resolution achieved by gantry rotation times down to 0.375 s and improved spatial resolution (NIEMAN 2002). As a consequence of the increased robustness of the technology, characterization and classification of coronary plaques are becoming feasible even in the presence of calcifications (ROPERS 2003).

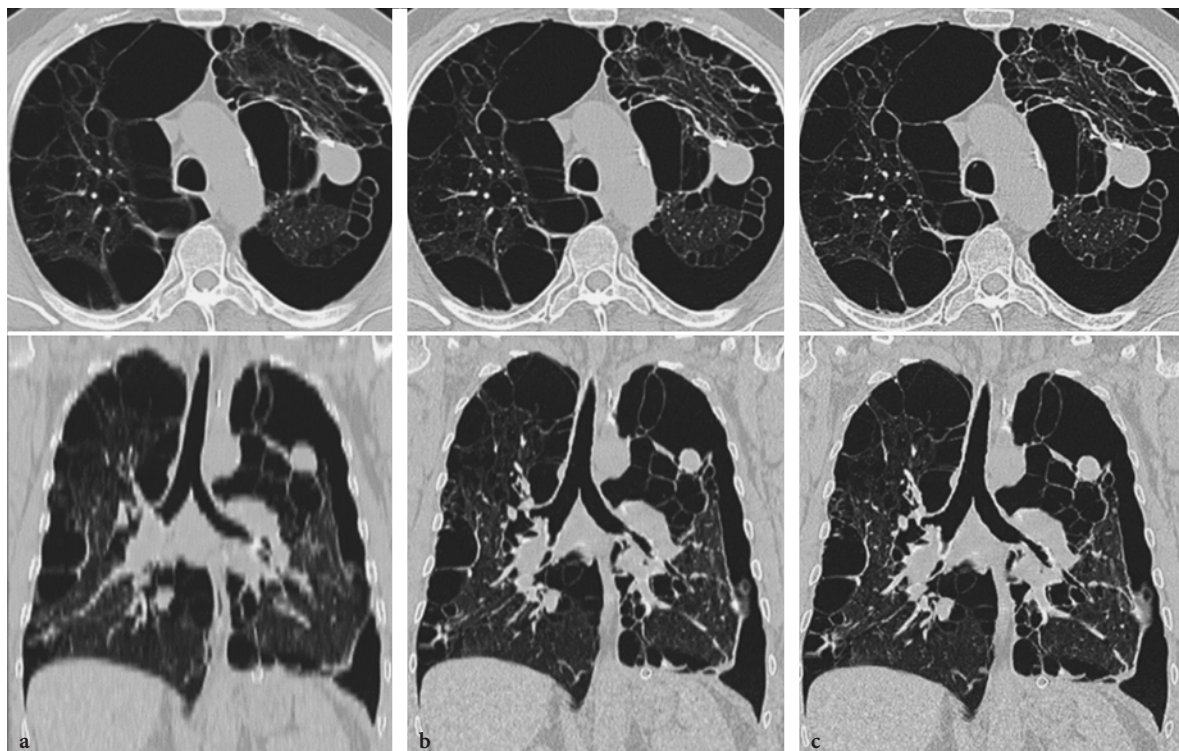


Fig. 3.2a–c. Case study consisting of axial slices and coronal multi-planar reformations (MPRs) of a thorax examination illustrating the clinical performance of a single-slice CT (7-mm slices, 30 s), **b** 4-slice CT (1.25-mm slices, 30 s) and **c** 16-slice CT (0.75-mm slices, 10 s). The difference in diagnostic image quality is most obvious in the MPRs. The single-slice and 4-slice images were synthesized from the 16-slice CT data. (Case courtesy of the Medical University of South Carolina, Charleston, USA)

Currently, the race for more slices is on-going. In 2004, all major CT manufacturers introduced the next generation of multi-slice CT systems, with 32, 40, and even 64 simultaneously acquired slices, which brought about a further leap in volume coverage speed. Whereas most of the scanners increase the number of acquired slices by increasing the number of the detector rows, some of the new scanners use additional refined z-sampling techniques with a periodic motion of the focal spot in the z-direction (z-flying focal spot). This so-called double z-sampling technique can further enhance longitudinal resolution and image quality in clinical routine (FLOHR 2003). With gantry rotation times down to 0.33 s, temporal resolution for ECG-gated examinations is again markedly improved. The progress in longitudinal spatial resolution from 4-slice to 64-slice CT can best be demonstrated with a z-resolution phantom, which

consists of a Lucite plate with rows of cylindrical holes of different diameters aligned in the z-direction. The 4-slice CT scanner with 4×1 -mm collimation can resolve 0.8-mm objects. With 16×0.75 -mm collimation, 0.6-mm objects can be delineated. The latest 64-slice CT scanner technology using 0.6-mm collimation and double z-sampling can routinely resolve 0.4mm objects, as demonstrated in Figure 3.3.

The most recent generation of CT systems will make CT angiographic examinations with sub-millimeter resolution feasible in the pure arterial phase even for extended anatomical ranges. CT angiography of the carotid arteries and the circle of Willis with 64×0.6 -mm slice, 0.375-s rotation time, and pitch 1.5 requires only 5 s for a scan range of 350 mm, as shown in the clinical example in Figure 3.4. Whole-body sub-millimeter CT angiography with a 1500-mm scan range, 64×0.6 -mm slice, 0.375-s rotation

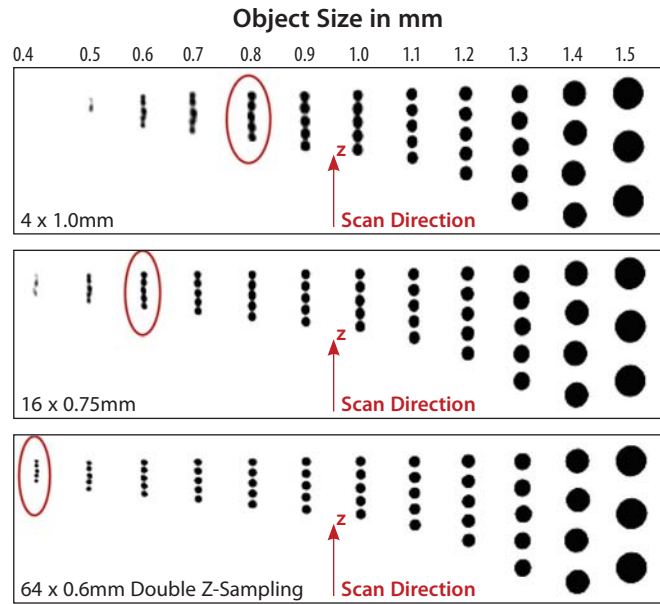


Fig. 3.3. Spatial resolution in the longitudinal (z-) direction for different multi-slice CT scanner technologies. A special resolution phantom containing cylindrical air-filled holes of different defined diameters in a Lucite plate was used. Whereas 16-slice CT scanners can resolve objects approximately 0.6 mm in size in the longitudinal direction, the latest 64-slice CT scanners employing “double z-sampling” techniques can resolve objects down to 0.4 mm size in this direction

time, and pitch of 1.2–1.4 will be completed in only 22–25 s (Fig. 3.5). Cardiac scanning will again benefit both from increased spatial and temporal resolution, facilitating the successful integration of CT coronary angiography into routine clinical algorithms. The improved temporal resolution obtained with a gantry rotation time of 0.33 s has the potential to increase clinical robustness at higher heart rates, thereby significantly reducing the number of patients requiring heart-rate control.

Table 3.1 shows examples of scan protocols for different generations of CT scanners for illustration. Very useful up-to-date information regarding multi-detector row CT is also readily available on the Internet, for example, at the UK MDA CT website (www.medical-devices.gov.uk or at www.ctisus.org).

3.2 Principles of Multi-slice CT System Design

The fundamental demands on a modern multi-slice CT scanner for large-volume coverage can be summed up in the following two requirements:

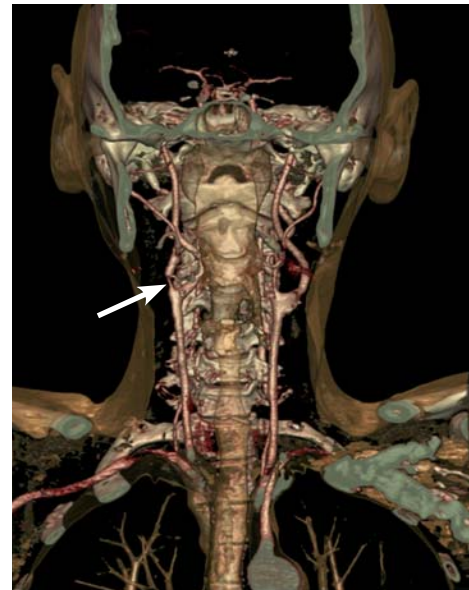


Fig. 3.4. Clinical example of a CT angiography of the carotid arteries and the circle of Willis in 3D volume-rendering display to illustrate the performance of the new 64-slice CT scanners with z-flying focal spot. Scan parameters: 120 kV, 150 effective mAs, 0.6-mm collimation, 0.375-s gantry rotation time, pitch 1.4, scan time 6 s for 350-mm scan range. The arrow indicates a severe carotid artery stenosis. (Case courtesy of the University of Erlangen, Germany)

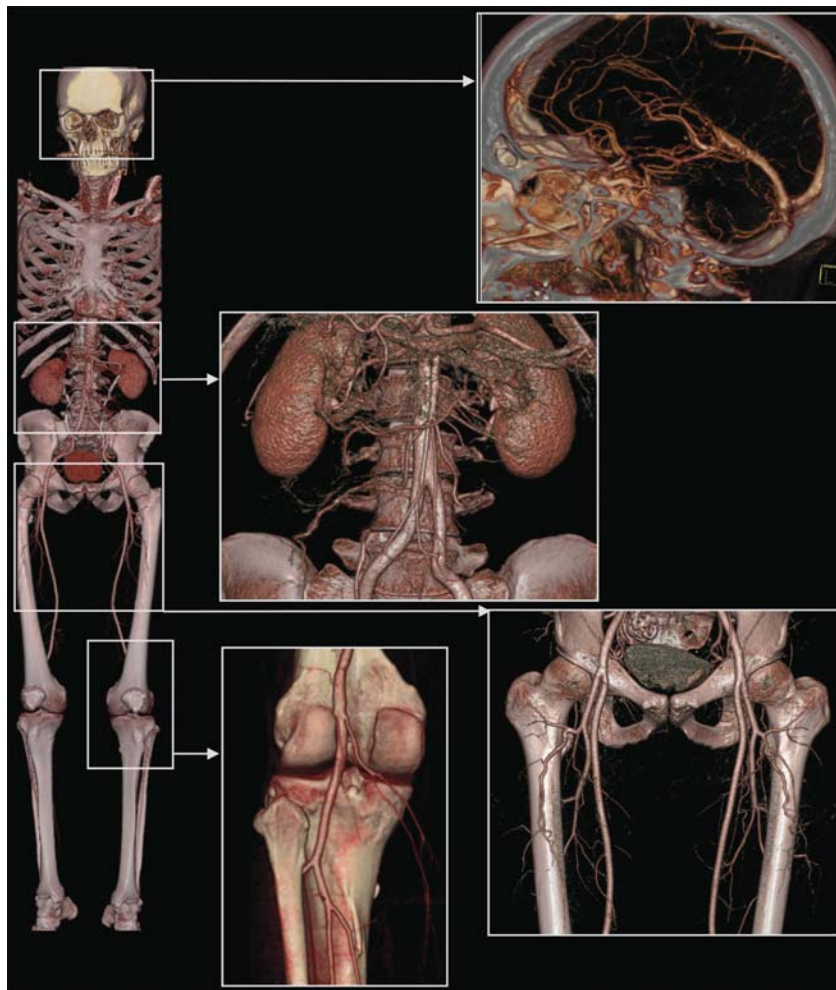


Fig. 3.5. Example of a whole-body CT angiography examination using a 64-slice CT with z-flying focal spot. Blow-up displays of the individual anatomical regions demonstrate the uncompromised regional resolution. Scan parameters: 120 kV, 150 effective mAs, 0.6 mm collimation, 0.375-s gantry rotation time, pitch 1.4, scan time 24 s for 1570-mm scan range. (Case courtesy of the University of Erlangen and the University of Tübingen, Germany)

Table 3.1. Scan protocols for thorax scans for different generations of CT scanners. With older single-slice CT scanners, users had to trade-off longitudinal resolution in favor of scan speed

	Collimation	Rotation time	Typical scan time for 35-cm range
Single-slice spiral (1992)	e.g., 1 mm	e.g., 0.75 s	175 s
	e.g., 10 mm	e.g., 0.75 s	17.5 s
Four slice (1998)	e.g., 4 × 1 mm	e.g., 0.5 s	29 s
16-slice (2001)	e.g., 16 × 0.75 mm	e.g., 0.5 s	10 s
64-slice (2003)	e.g., 64 × 0.6-mm sampled at 0.3 mm	e.g., 0.33 s	5 s

1. Continuous data acquisition (the possibility to reconstruct images at any z position)
2. Ability to scan a long range in a short time without compromising longitudinal (z) resolution

The first requirement calls for a spiral acquisition. The breakthrough in multi-slice spiral CT brought about in 1998 was due to the fact that it was able to fulfill the second requirement: maximum z resolution is defined by the longitudinal detector pixel size alone rather than by a combination of spiral pitch and detector collimation as in single-slice spiral scanners. Moreover, multi-slice spiral scanners provide the new feature of allowing the z -resolution to be specified in the image-reconstruction step, i.e., after the scan has been done.

The technical challenges of multi-slice CT are manifold: A detector capable of measuring several thousand channels at a time has to be built; the data have to be transferred to the image-reconstruction system, and a suitable reconstruction algorithm has to be provided.

The basic system components of a modern “third-generation” CT system are shown in Figure 2.2. Third-generation CT scanners employ a “rotate/rotate” geometry, in which both the X-ray tube and the detector rotate about the patient (Fig. 2.2d). In a multi-slice CT system, the detector comprises many rows of 700 and more detector elements that cover a scan field of view (SFOV) of usually 50 cm. The X-ray attenuation of the object is measured by the individual detector elements. Each measurement value is characterized by: (1) its projection angle α , i. e., the angular coordinate of the line connecting the center of the detector and the focal spot of the X-ray tube; (2) the fan angle β , i. e., the angle between each individual detector element and this center-line; and (3) the slice-index m . All measurement values acquired at the same angular position of the measurement system, that is, at the same α , are called a projection of view. Typically, 1000 projections are measured during each 360° rotation. An alternative set of variables characterizing the measurement rays is θ , b , and m , where θ is the azimuthal angle and b denotes the distance of a ray from the iso-center (Fig. 3.6). α and β are used when projection data are in the form of fan-beam projections, θ and b are used to label rays when projection data are in the form of parallel

projections. Most modern CT scanners use “rebinning”, which is an interpolation of the measured fan-beam data to parallel data, since parallel geometry simplifies image reconstruction.

The overall performance of a CT system depends on several key components. These include the X-ray source; a high-powered generator, detector, and detector electronics; data transmission systems (slip-rings); and the computer system for image reconstruction and manipulation.

State-of-the-art X-ray tube/generator combinations provide a peak power of 60–100 kW, usually at various user-selectable voltages, e. g., 80, 100, 120, and 140 kV. Different clinical applications require different X-ray spectra and hence different kV settings for optimum image quality and/or best possible signal-to-noise ratio at the lowest radiation dose. As an example, CT angiographic examinations generally benefit from a lower tube voltage (SCHÖPF 2003). In a conventional tube design, an anode plate that is typically 160–220 mm in diameter rotates in a vacuum housing (Fig. 3.7a). The heat-storage capacity of the anode plate and tube housing – measured in mega heat units (MHU)–determines the performance level: the bigger the anode plate is, the larger the heat-storage capacity, and the more scan-seconds can be delivered until the anode plate reaches its temperature limit. Typically, a conventional state-of-the-art X-ray tube has a heat-storage capacity of 5–9 MHU, realized by thick graphite layers attached to

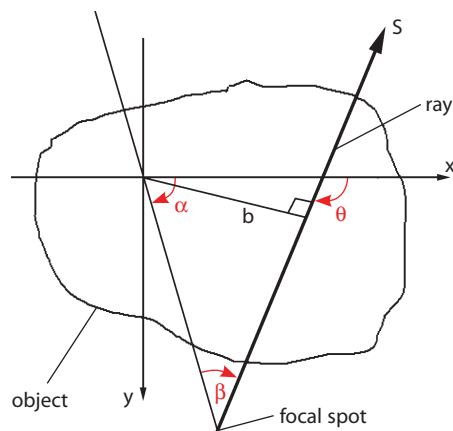


Fig. 3.6. Definition of variables used to characterize the measurement rays of a CT scanner. A parallel projection is obtained by assembling rays from several fan-beam projections

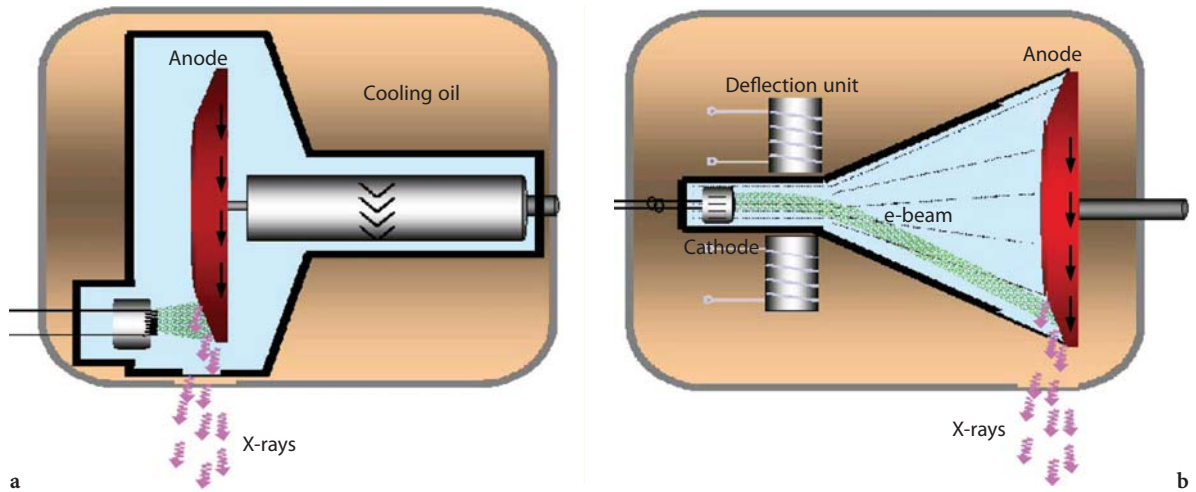


Fig. 3.7. A conventional X-ray tube (a) and a rotating-envelope tube (b). The electrons emitted by the cathode are represented by green lines, the X-rays generated in the anode are depicted as purple arrows. In a conventional X-ray tube, the anode plate rotates in a vacuum housing. Heat is mainly dissipated via thermal radiation. In a rotating-envelope tube, the anode plate constitutes an outer wall of the tube housing and is in direct contact with the cooling oil. Heat is effectively dissipated via thermal conduction, and the cooling rate is significantly increased. Rotating-envelope tubes have no moving parts and no bearings in the vacuum

the backside of the anode plate. The heat produced in the anode during X-ray emission is mainly dissipated via thermal radiation, with only a small percentage released via thermal conduction (Fig. 3.7a). The moderate heat dissipation rates of 0.5–1.8 MHU/min usually limit the rate at which scans can be repeated as well as the maximum available power for each scan. Constructive efforts aim at increasing both the heat-storage capacity and the heat-dissipation rate, e.g., by increasing the anode diameter, using circular grooves in the anode support to increase the contact area for improved cooling, or by employing special liquid-metal vacuum bearings that allow for faster anode rotation. An alternative design is the so-called rotating-envelope tube, as illustrated in Figures 3.7b and 3.8. The anode plate constitutes an outer wall of the rotating tube housing; it is therefore in direct contact with the cooling oil and can be effectively cooled by thermal conduction. In this way, a very high heat-dissipation rate of 5 MHU/min is achieved, eliminating the need for heat storage in the anode, which consequently has a heat-storage capacity close to zero. Due to the rapid cooling of the anode, rotating-envelope tubes can perform high-power scans in rapid succession. With rotating-envelope tubes,

up to five full-power 10-s spirals are possible within 100 s (SCHARDT 2004). Ultimately, the performance of both conventional and rotating-envelope tubes is limited by the maximum heat dissipation of the CT system itself. Since there are no moving parts and no bearings in the vacuum, the tube design can be small and compact (anode diameter 12 cm) so that it

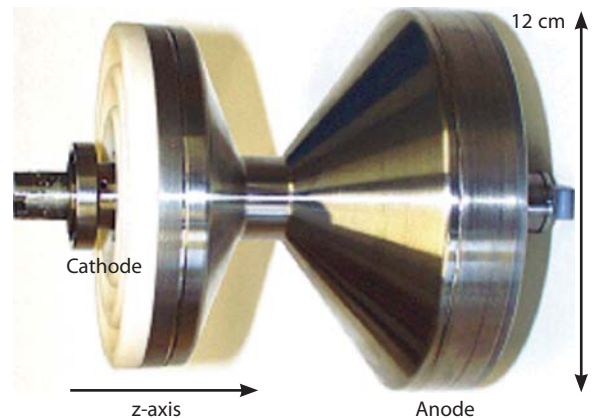


Fig. 3.8. A rotating-envelope X-ray tube (STRATON tube, Siemens, Forchheim, Germany). The tube design is very compact; the anode diameter is only 12 cm

has the potential to better withstand the high gravitational forces associated with gantry rotation times of < 0.4 s. Due to the central rotating cathode, permanent electromagnetic deflection of the electron beam is needed to position and shape the focal spot on the anode. Versatile electromagnetic deflection is a prerequisite for the flying focal spot in the z-direction that has been used in most of the recent 64-slice CT-systems.

With the increasing number of detector rows and decreasing gantry rotation times, the data-transmission systems of multi-slice CT scanners must be capable of handling significant data rates. A 4-slice CT-system with 0.5-s rotation time roughly generates $1000 \times 700 \times 4 \times 2$ Bytes = 5.6 MB of data per rotation, corresponding to 11.2 MB/s; a 16-slice CT-scanner with the same rotation time generates 45 MB/s, and a 64-slice CT-system can produce up to 180–200 MB/s. This stream of data is a challenge for data transmission off the rotating part of the gantry and for real-time data processing in the subsequent image-reconstruction systems. In modern CT systems, contactless transmission technology is generally used for data transfer; that is, either laser transmission or electromagnetic transmission with coupling between a rotating transmission ring antenna and a stationary receiving antenna. In the image-reconstruction, computer images are reconstructed at a rate of up to 40 images/s using special array processors.

Modern CT systems generally use solid-state detectors. Each detector element consists of a radiation-sensitive solid-state material (such as cadmium tungstate, gadolinium-oxide, or gadolinium oxysulfide with suitable dopings), which converts the absorbed X-rays into visible light. The light is then detected by a silicon photodiode. The resulting electrical current is amplified and converted into a digital signal. Key requirements for a suitable detector material are good detection efficiency and very short afterglow time to enable the fast gantry rotation speeds that are essential for ECG-gated cardiac imaging. Gas detectors, such as the xenon detectors used in previous generations of single-slice CT systems, have meanwhile become obsolete due to their limited detection efficiency.

A CT detector must provide different slice widths to adjust the optimum scan speed, longitudinal resolution, and image noise for each application. With a single-slice CT detector, different collimated slice widths are obtained by pre-patient collimation of the X-ray beam (Fig. 3.9). Figure 3.9 shows a very elementary model of a 2-slice CT detector consisting of two detector rows generating 2 slices per rotation. Different slice widths are obtained by pre-patient collimation as the detector is separated midway along the z-extent of the X-ray beam.

For acquisition of more than 2 slices per rotation, this simple design principle must be replaced by a more flexible one, in which the number of detector

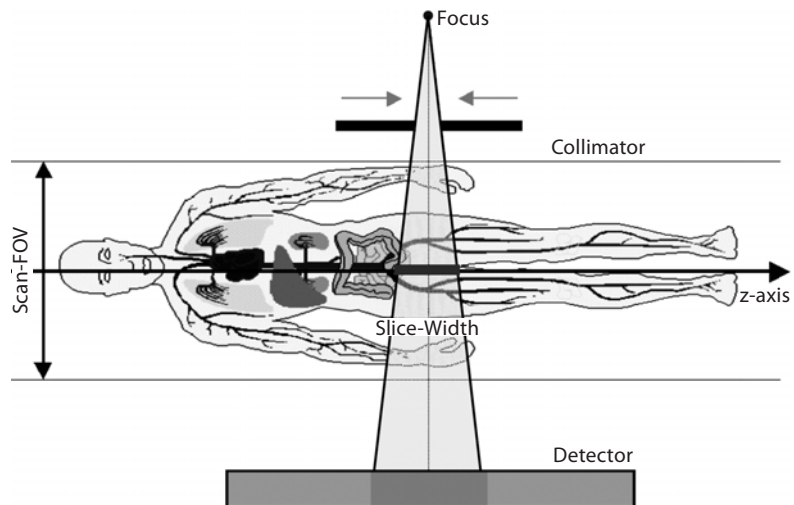


Fig. 3.9. Pre-patient collimation of the X-ray beam to obtain different collimated slice widths with a single-slice CT detector or a dual-slice CT detector

rows is greater than the number of simultaneously acquired slices. In order to be able to select different slice widths, several detector rows are electronically combined into a smaller number of slices according to the selected beam collimation and the desired slice width.

For the 4-slice CT systems introduced in 1998, two detector types have been commonly used. The fixed array detector consists of detector elements with equal sizes in the longitudinal direction. A representative example for this scanner type has 16 detector rows, each of them defining a collimated slice width in the center of rotation of 1.25 mm (Hu 1999, Hu 2000, McCOLLOUGH 1999). The total coverage in the longitudinal direction is 20 mm at iso-center; due to geometric magnification, the actual detector is about twice as wide. By pre-patient collimation and combination of the signals of the individual detector rows, the following slice widths (measured at iso-center) are realized: 4×1.25 , 4×2.5 , 4×3.75 , and 4×5 mm (Fig. 3.10a). The same detector design can be used for an 8-slice version of this system, with collimated slice widths of 8×1.25 and 8×2.5 mm.

A different approach uses an adaptive array detector design, which comprises detector rows with different sizes in the longitudinal direction. Scanners of this type have eight detector rows that can be combined to yield different slice-collimation settings (KLINGENBECK 1999, OHNESORGE 1999). Slice widths in the longitudinal direction range from 1 to 5 mm (at iso-center) and allow for the following collimated slice widths: 2×0.5 , 4×1 , 4×2.5 , 4×5 , 2×8 , and 2×10 mm (Fig. 3.10b).

The selection of the collimated slice width determines the intrinsic longitudinal resolution of a scan. In a "step-and-shoot" axial mode, any multiple of the collimated width of one detector slice can be obtained by adding the detector signals during image reconstruction. In a spiral mode, the effective slice width – which is usually defined as the full width at half maximum (FWHM) of the spiral slice sensitivity profile (SSP) – is adjusted independently in the spiral interpolation process during image reconstruction. Hence, from the same data set, both narrow slices for high-resolution detail or 3D post-processing and wide slices for better contrast resolution or quick review and filming may be derived.

The established 16-slice CT systems generally have adaptive array detectors. One representative example for this scanner type uses 24 detector rows (FLOHR 2002). The 16 central rows define a 0.75-mm collimated slice width at iso-center; the four outer rows on both sides define a 1.5-mm collimated slice width (Fig. 3.10c). The total coverage in the longitudinal direction is 24 mm at iso-center. By appropriate combination of the signals of the individual detector rows, either 12 or 16 slices, each with a collimated slice width of 0.75 mm or 1.5 mm, can be acquired simultaneously. Most commercially available 16-slice CT scanners use similar detector designs, partly with different collimation settings (e.g., 16×0.625 mm/ 16×1.25 mm or 16×0.5 mm/ 16×1 mm/ 16×2 mm collimated slice width).

In 2004, the latest generation of multi-slice CT systems providing more than 16 slices, up to 64 slices per rotation, was introduced. One of the new scanners employs an adaptive array detector with a total of 40 detector rows and a special double z-sampling technique that doubles the number of slices acquired per rotation. The 32 central detector rows of this scanner define a 0.6-mm collimated slice width at iso-center; the four outer rows on both sides define a 1-mm collimated slice width (Fig. 3.10d). When all 40 detector rows are illuminated, the total coverage in the longitudinal direction is 28.8 mm. Using a periodic motion of the focal spot in the z-direction (z-flying focal spot), two subsequent 32-slice readings with a collimated slice width of 0.6 mm are slightly shifted in the z-direction and combined to yield one 64-slice projection with a sampling distance of 0.3 mm at iso-center. With this double z-sampling technique, 64 overlapping 0.6-mm slices per rotation are acquired. Alternatively, 24 slices, each with a 1.2-mm slice width, can be obtained to provide the full longitudinal detector coverage of 28.8 mm.

Another 40-slice system design provides 40 slices based on an adaptive array detector design with 40×0.625 -mm or 32×1.25 -mm collimation, with a coverage of 40 mm at iso-center (Fig. 3.10e). Other recently introduced 64-slice scanners employ fixed array detectors with 64 detector rows, with a thinnest collimated slice width of 0.5–0.625 mm, thus providing a total volume coverage of 32–40 mm (Fig. 3.10f). A direct comparison of the two different 64-slice detec-

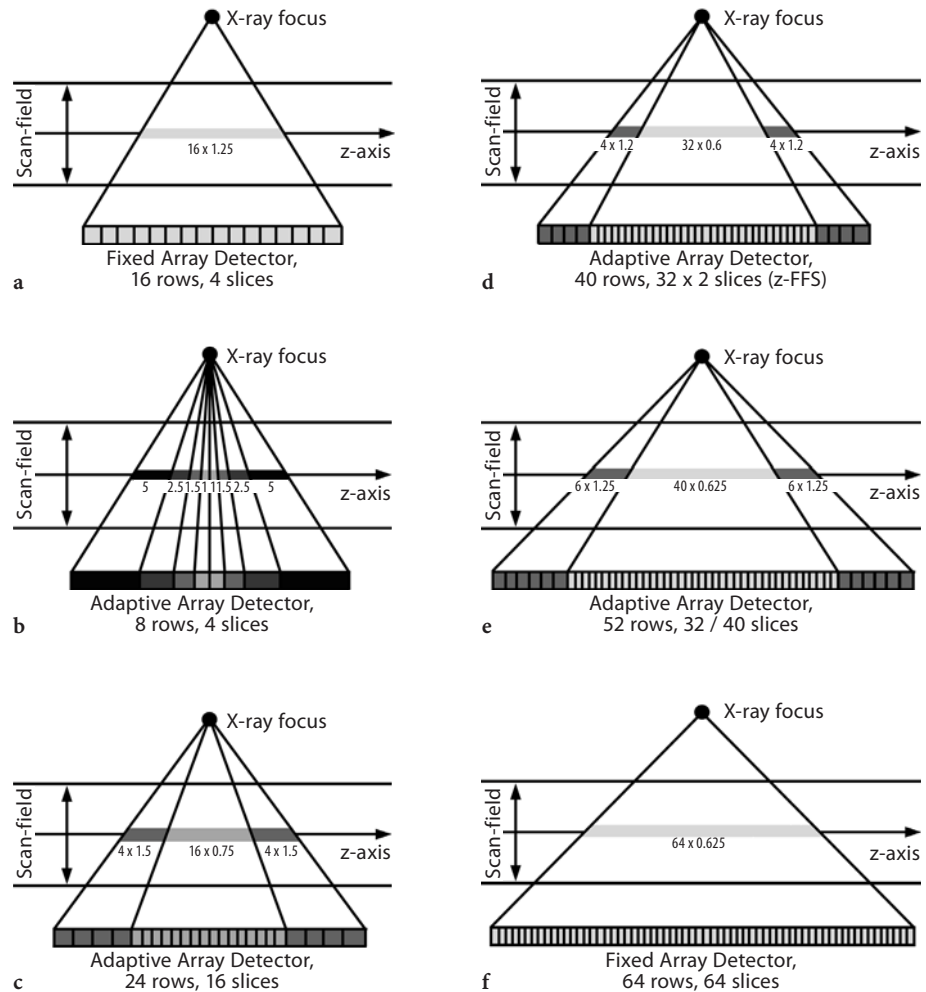


Fig. 3.10a–f. Examples of fixed array detectors and adaptive array detectors used in commercially available multi-slice CT systems. **a** Fixed array detector of a 4- to 8-slice CT scanner, GE LightSpeed Plus and Ultra; **b** adaptive array detector of a 4-slice CT scanner (Siemens SOMATOM Sensation 4 and Philips MX 8000); **c** adaptive array detector of a 16-slice CT scanner (Siemens SOMATOM Sensation 16 and Philips MX 8000 IDT); **d** adaptive array detector of a 64-slice CT scanner employing double z-sampling technique (Siemens SOMATOM Sensation 64); **e** adaptive array detector of a 40-slice CT scanner (Philips Brilliance 40); **f** fixed array detector of a 64-slice CT scanner using 64 detector rows (GE LightSpeed VCT and Philips Brilliance 64)

tor designs with 32 rows and double z-sampling vs. straight 64-row geometry is shown in Figure 3.11a–c. Whereas the straight 64-row concept can acquire four times more volume per rotation with sub-millimeter slices than the previous 16-slice CT scanners, double z-sampling can still allow the acquisition of two times more volume per rotation but also twice the amount of data per volume. This results in

improved resolution and image quality compared to previous 16-slice CT scanners. Figure 3.11d shows a representative example of a detector module of a 64-slice CT scanner that employs the double z-sampling technique. Each module consists of 40×16 detector pixels and the corresponding electronics. The anti-scatter collimators are diagonally cut to open the view of the detector ceramics.

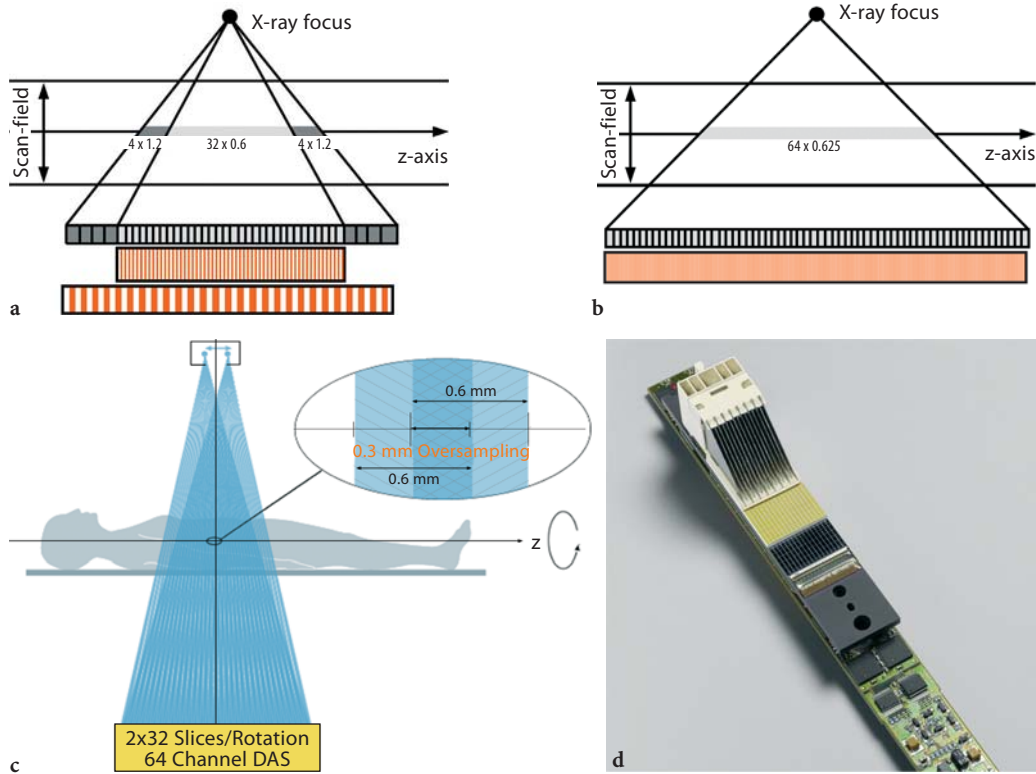


Fig. 3.11. Direct comparison of two different 64-slice detector designs shows that the 32-row design with double z-sampling (a) acquires double the amount of data per volume compared to a straight 64-row geometry (b). The double z-sampling technique with 0.6-mm detector collimation provides data samples at 0.3-mm sampling distance in the z-direction (c). A detector module of a 64-slice CT scanner using the double z-sampling technique (Siemens SOMATOM Sensation 64) is shown in (d). Each module consists of 40×16 detector pixels with the corresponding electronics. The anti-scatter collimators are diagonally cut to open the view on the detector ceramics (yellow)

3.3

Multi-slice CT Acquisition and Reconstruction for Body Imaging

With the advent of multi-slice CT, axial sequential scanning ("step-and-shoot" scanning) has remained in use only for few clinical applications, such as standard head scanning, high-resolution lung scanning, perfusion CT, and interventional applications. A detailed theoretical description to predict the performance of multi-slice CT in sequential mode can be found in (HSIEH 2001). However, spiral (or "helical") scanning is the method of choice for the vast majority of multi-slice CT examinations.

3.3.1

Definition of the Pitch

An important parameter to characterize a spiral/helical scan is the pitch. According to IEC (International Electrotechnical Commission 2002) specifications, the pitch is given by:

$$\text{pitch} = \text{table feed per rotation} / \text{total width of the collimated beam} \quad (3.1)$$

This definition holds for single-slice CT and for multi-slice CT. It shows whether data acquisi-

tion occurs with gaps (pitch > 1) or with overlap (pitch < 1) in the longitudinal direction. For a 4-slice CT scanner with 4×1 -mm collimation and a table-feed of 6 mm per rotation, pitch = $6/(4 \times 1) = 6/4 = 1.5$. With 16×0.75 -mm collimation and a table-feed of 18 mm/rotation, pitch = $18/(16 \times 0.75) = 18/12 = 1.5$, too. In the early days of 4-slice CT, the term “detector pitch” was additionally introduced, and it accounts for the width of one single slice in the denominator. For a beam collimation of 4×1 mm, the beam consists of four sub-beams, each 1-mm wide at the center of rotation. With 6-mm table-feed per rotation, the detector pitch is $\text{pitch}_{vol} = 6/1 = 6$. For the sake of clarity, the detector pitch should no longer be used.

3.3.2 The Cone-Angle Problem in Multi-slice CT

The 2D image-reconstruction approaches used in commercially available, single-slice CT scanners require that all measurement rays contributing to an image run in a plane perpendicular to the patient’s longitudinal axis. In multi-slice CT systems, this requirement is violated. For illustration of the cone-beam effect, Figure 3.12 shows the geometry of a 4-slice scanner in an exaggerated manner. The measurement rays are tilted by the so-called cone-angle with respect to the center plane. The cone-angle is largest for the slices at the outer edges of the detector and it increases with an increasing number of detector rows if their width is kept constant. As a first approximation, the cone-angle is neglected in multi-slice CT reconstruction approaches. Then, the measurement rays are treated as if they travel perpendicular to the z-axis, and modified two-dimensional image-reconstruction algorithms are used. The data, however, are then inconsistent, and cone-beam artifacts will be produced. These are most pronounced at high-contrast structures and increase with increasing distance of the object from the iso-center. Typical sources of cone-beam artifacts in medical images are the ribs or the pelvic bones (Fig. 3.13).

It has been demonstrated that cone-beam artifacts can be tolerated if the slice blurring δS does not exceed the half-slice collimation $SW_{coll}/2$

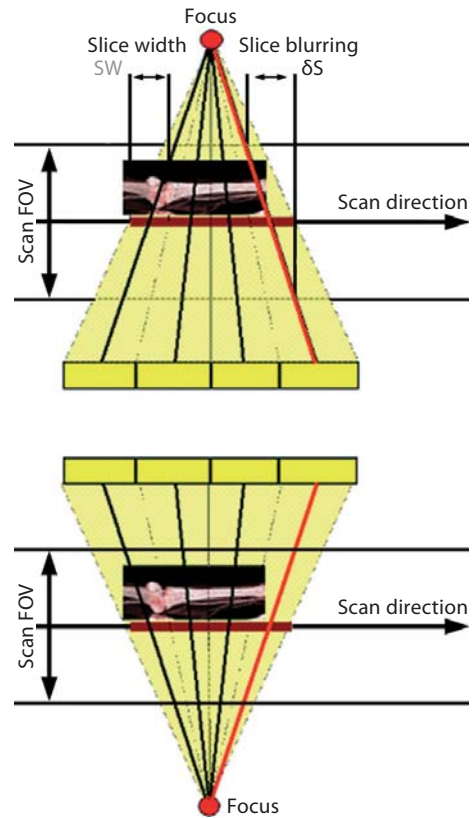


Fig. 3.12. Geometry of a 4-slice CT scanner demonstrating the cone-angle problem: the measurement rays are tilted by the so-called cone-angle with respect to the center plane. Top and bottom Two different view angles in an axial scan that are shifted by 180° so that the positions of X-ray tube and detector are interchanged. With a single-slice CT system, identical measurement values would be acquired whereas with a multi-slice CT system, different measurement values are acquired

(KLINGENBECK 1999, OHNESORGE 1999, OHNESORGE 2001) (for definitions, see Fig. 3.12). This condition holds generally true if the maximum number N of simultaneously acquired slices does not significantly exceed $N = 4$ (SAITO 1998). As a consequence, the image-reconstruction approaches of all commercially available CT-systems with 4–6 slices, and of some with even more slices, neglect the cone-angle of the measurement rays and either extend 180° or 360° single-slice spiral interpolation techniques to multi-slice spiral scanning (180° or 360° multi-slice

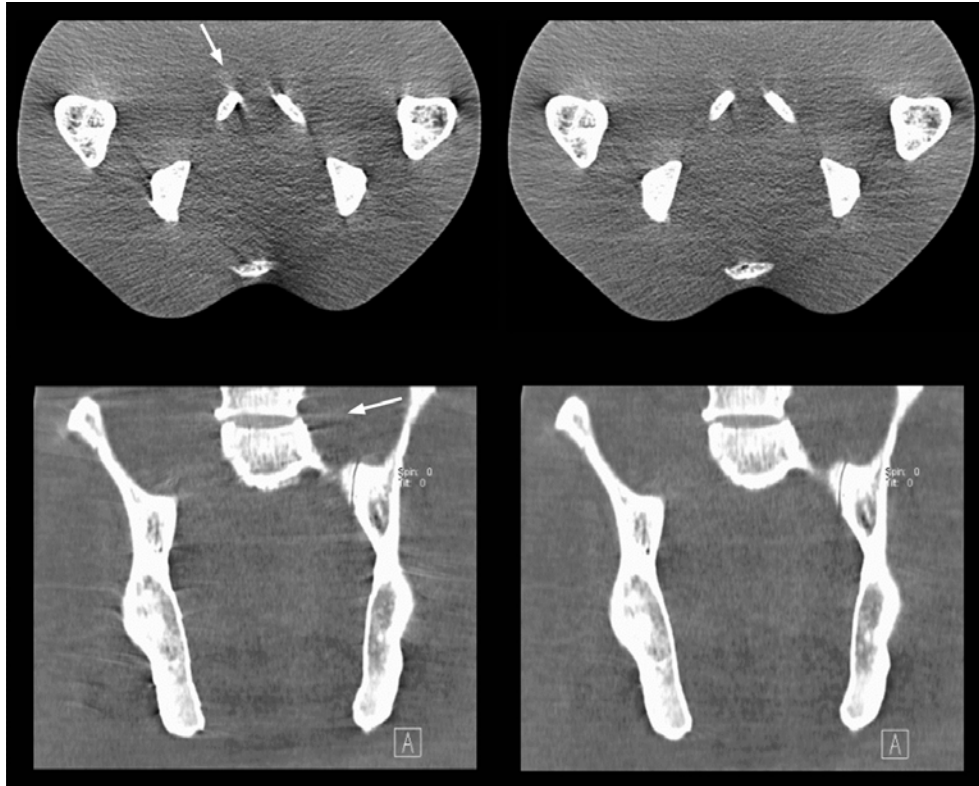


Fig. 3.13. Typical cone-beam artifacts demonstrated for a CT system with 16×1.5 -mm collimation. Axial slice (*top*) and MPR (*bottom*) for a spiral scan of a pelvic phantom at pitch 1. Left Conventional multi-slice spiral reconstruction neglecting the cone-angle of the measurement rays. Cone beam-artifacts at the pelvic bones are indicated by *arrows*. Right Cone-beam reconstruction adaptive multiple plane reconstruction (AMPR). Cone-beam artifacts are suppressed

linear interpolation; see HU 1999) or they introduce generalized z-filter approaches (TAGUCHI 1998, SCHALLER 2000). While these approaches are fully adequate for 4–6 slice CT scanners, they will lead to artifacts and image-quality degradation if applied to spiral scanning with 16 and more slices. In this context, ECG-gated cardiac scanning requires special attention. The heart is usually sufficiently centered and does not contain extended high-contrast structures that could be the source of cone-beam artifacts. Indeed, adequate results without cone correction are obtained for cardiac scanning with 16 slices; only with 64 slices do cone-beam reconstruction approaches also become mandatory for ECG-gated spiral CT (FLOHR 2003) (Fig. 3.14).

3.3.3

Multi-slice Spiral Reconstruction Neglecting the Cone-Beam Geometry

3.3.3.1

180° and 360° Multi-slice Linear Interpolation

The 360° and 180° linear interpolation (LI) single-slice spiral reconstruction approaches can be extended to multi-detector row spiral scanning in a straightforward way (HU 1999, SCHALLER 2000, HSIEH 2003). Both 360° and 180° multi-slice linear interpolation (MLI) are characterized by a projection-wise linear interpolation between two rays on either side of the image plane. The cone-angle of

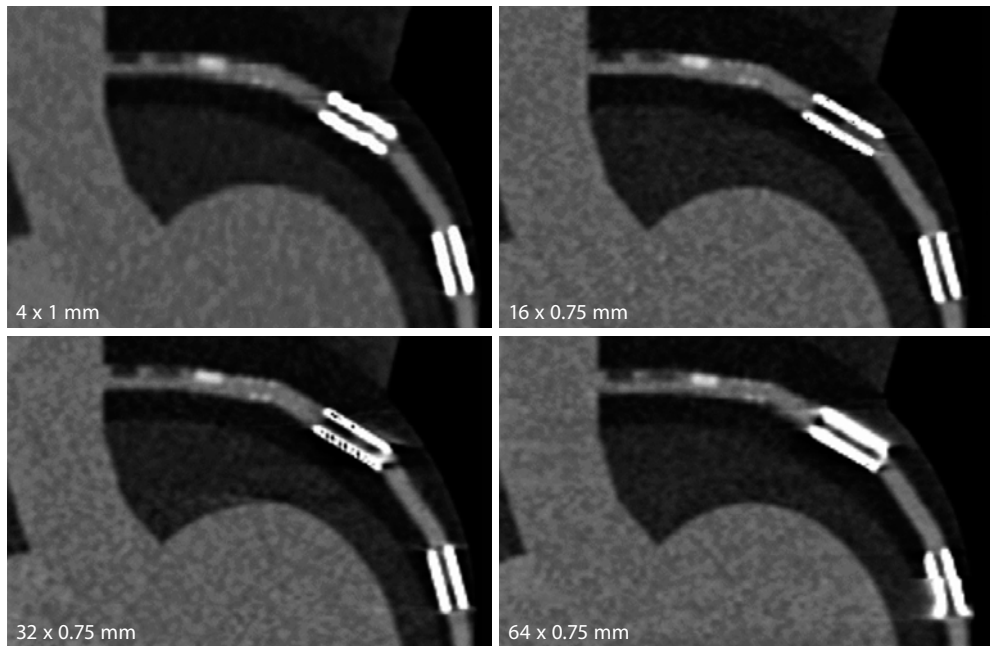


Fig. 3.14. Cone-beam artifacts in cardiac CT. MPRs along the left anterior descending (LAD) coronary artery of an anthropomorphic heart phantom for virtual scanner geometries with collimations of 4×1 , 16×0.75 , 32×0.75 , and 64×0.75 mm. ECG-gated reconstruction neglecting the cone-angle of the measurement rays. Deviating from general radiology applications, the MPRs show no significant cone-beam artifacts for up to 16 slices. For 32 slices, the MPRs begin to suffer from such artifacts; see the stents in the LAD. For 64 slices, MPRs show severe cone-beam artifacts

the measurement rays is not taken into account. In the 360° MLI spiral reconstruction approach, either rays measured at the same projection angle by different detector rows or rays measured in consecutive rotations of the scanner (i.e., 360° apart) are used for spiral interpolation. In the 180° MLI spiral reconstruction approach, both direct and complementary rays are considered. At iso-center, direct and complementary rays interleave in the z-direction for selected pitch values. In this way, the distance between measured samples is significantly reduced and equals half the collimated slice width, SW_{coll} , which results in the desired narrow SSPs. Appropriate pitch values are 0.75 for 4-slice scanning (HU 1999) and 0.5625 or 0.9375 for 16-slice scanning (HSIEH 2003). Figure 3.15 schematically illustrates 180° and 360° MLI for the example of a 4-slice CT scanner.

In general, scanners relying on 180° or 360° MLI techniques and extensions thereof provide selected

discrete pitch values to the user – such as 0.75 and 1.5 for 4-slice scanning (HU 1999), or 0.5625, 0.9375, 1.375, and 1.75 for 16-slice scanning (HSIEH 2003). The user has to be aware of pitch-dependent effective slice widths (s). For low-pitch scanning (at pitch = 0.75 using 4 slices and at pitch = 0.5625 or 0.9375 using 16 slices), $SW \sim SW_{coll}$, and for a collimated 1.25-mm slice the resulting effective slice width stays at 1.25 mm. The narrow SSP, however, is achieved by a 180° MLI reconstruction using conjugate interpolation at the price of increased image noise (HU 1999, HSIEH 2003). For high-pitch scanning (at $p = 1.5$ using 4 slices and at pitch = 1.375 or 1.75 using 16 slices), $SW \sim 1.27SW_{coll}$, and a collimated 1.25-mm slice results in an effective 1.5- to 1.6-mm slice. When comparing dose and image noise for different pitch values, widening of the SSP has to be taken into account. To obtain the same image noise as in an axial scan with the same collimated slice width, 0.73–1.68 times the dose depending on the spiral

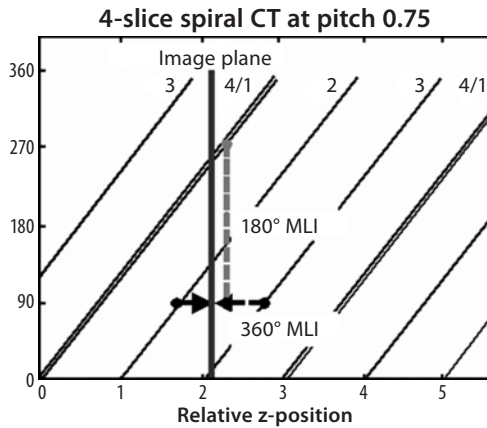


Fig. 3.15. Schematic illustration of 180° and 360° multi-slice linear interpolation (MLI) for a 4-slice CT system at pitch 0.75. The projection angle of the central channels of the 4 detector rows (in degrees) is indicated as a function of their relative z-positions (in multiples of the collimated slice width). In a full rotation (360°), the detector travels three collimated slice widths, and the z-positions that were sampled by detector row 4 are now again sampled by detector row 1. For 360° MLI, rays measured at the same projection angle are used; these may be either taken from subsequent rotations or from different detector rows in the same rotation. For the projection angle indicated in this example (90°), data from detector rows 2 and 3 are used, and the sampling distance equals the collimated slice width (two dark arrows). For 180° MLI, complementary rays from opposite directions are used; these are shifted by 180° in the center of rotation. In this example, the direct interpolation partner from row 3 at 90° is replaced by a complementary one from row 1 and row 4 at 270° (dashed light-gray line). The sampling distance is now half the collimated slice width, which results in the desired narrow slice sensitivity profile

pitch is required, with the lowest dose at the highest pitch (HSIEH 2003). Some manufacturers provide a semi-automatic adaptation of the mA value to keep the image noise constant if the pitch is changed. When selecting the scan protocol for a particular application, scanning at low pitch optimizes image quality and longitudinal resolution at a given collimation, yet at the expense of increased dose of radiation to the patient. To reduce patient dose, high pitch values should be chosen

3.3.3.2 z-Filter Approaches

In a z-filter multi-slice spiral reconstruction (TAGUCHI 1998, SCHALLER 2000), the spiral interpolation for each projection angle is no longer restricted to the two rays in closest proximity to the image plane. Instead, all direct and complementary rays within a selectable distance from the image plane contribute to the image. The weighting function for the rays is selectable, which allows adjustment of both the functional form and the FWHM of the spiral SSP. Still, the cone-angle is neglected. A representative example for a z-filter approach is the adaptive axial interpolation (SCHALLER 2000), which is illustrated in Figure 3.16. Another example is the MUSCOT algorithm (TAGUCHI 1998). With z-filtering, the system can trade-off z-axis resolution (SSP) for image noise (which directly correlates with required dose). With

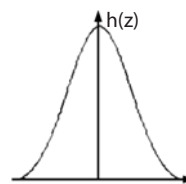
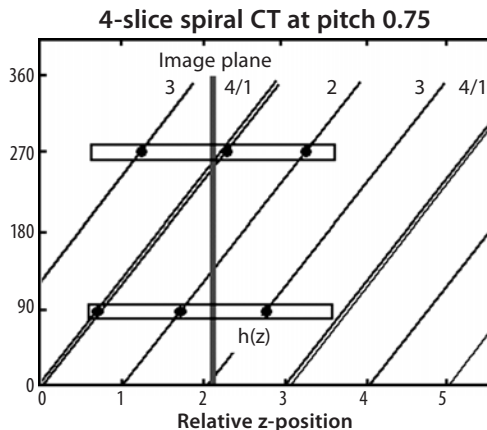


Fig. 3.16. A z-filter reconstruction (adaptive axial interpolation) for a 4-slice CT system at pitch 0.75 (similar to Fig. 3.14). Contributions from all projections at corresponding or opposite projection angles within a selectable distance from the image plane are used, as indicated by the two boxes at 90° and 270° . The weight of the contribution depends on the distance of the respective measurement ray from the image plane. The weighting function $h(z)$ (right) is selectable

the adaptive axial interpolation, the spiral pitch is freely selectable in the range 0.5–2.0, and the same effective slice width, defined as the FWHM of the spiral SSP, is generated at all pitch values (KLINGENBECK 1999, SCHALLER 2000, FUCHS 2000). Therefore, longitudinal resolution is independent of the pitch, deviating from single-slice spiral CT and from multi-slice CT relying on 180° and 360°MLI (HU 1999, HSIEH 2003). Figure 3.17 shows the SSPs of the 2-mm slice (for 4 × 1-mm collimation) and MPRs of a spiral z-resolution phantom for selected pitch values. As a consequence of the pitch-independent spiral slice width, the image noise for fixed mA (fixed tube current) would decrease with decreasing pitch due to the increasingly overlapping spiral acquisition. Instead, the user selects an “effective” mAs value, and the tube current (mA) is then automatically adapted to the pitch of the spiral scan to compensate for dose accumulation. The dose for fixed effective

mAs is independent of the spiral pitch and equals the dose of an axial scan with the same mAs.

In conclusion, when using z-filter multi-slice spiral reconstruction approaches, changing the pitch in multi-slice CT does not change the radiation dose to the patient, which is not the case in single-slice spiral CT. Accordingly, using higher pitch in multi-slice CT does not result in dose reduction, which is an important practical consideration with CT systems, in particular those applying adaptive axial interpolation reconstruction algorithms.

The intrinsic resolution of a multi-slice spiral CT scan is determined by the choice of collimation, e.g., 4 × 1 or 4 × 2.5-mm. With z-filtering, retrospective reconstruction of images with different slice widths from the same CT raw data set is possible. Only slice widths equal to or larger than the collimation of one slice can be obtained. In many cases, both thick slices for initial viewing and filming and thin slices

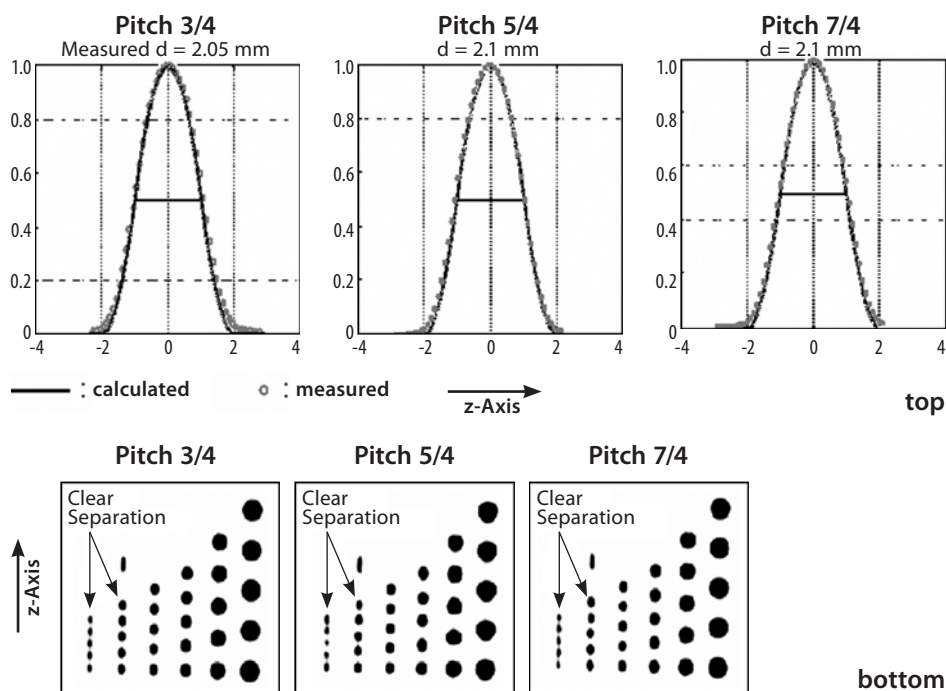


Fig. 3.17. Adaptive axial interpolation for a 4-slice CT-system. Top Slice sensitivity profiles (SSPs) of the 2-mm slice (for 4 × 1-mm collimation) at selected pitch values. The functional forms of the SSPs, and hence the slice widths, are independent of the pitch. Bottom MPRs of a spiral z-resolution phantom scanned with 2-mm slice width show clear separation of the 1.5- and 2-mm cylinders for all pitch values as a consequence of the pitch-independent SSPs

for detail diagnosis or as an input for advanced 3D post-processing are routinely reconstructed. For a 1.25-mm spiral slice width reconstructed from a 4×1 -mm collimation, only a factor 0.61–0.69 of the dose is required to maintain the image noise of an axial scan at the same collimation, depending only slightly on the spiral pitch (FUCHS 2000). In contrast to 180° and 360° MLI, image noise is therefore practically independent of the pitch at constant dose.

For optimum image quality, a narrow collimation relative to the desired slice width is preferable (SCHALLER 2000). Except for a minor dose increase due to the different relative contributions of the penumbra zones of the dose profile, scanning at narrow collimation does not result in a higher radiation dose to the patient, as long as the effective mAs is kept constant. Narrow collimation scanning should therefore be the protocol of choice for all applications that require 3D post-processing as part of the clinical evaluation. In the clinical management of uncooperative patients or trauma victims, or for protocols such as routine oncological staging, the use of wider collimation can be considered. Optimal suppression of spiral artifacts is achieved by using narrow collimation relative to the desired slice width and by reducing the spiral pitch. In general, more challenging clinical protocols, such as examinations of the spine and base of the skull, rely on a combination of narrow collimation and low pitch.

Some manufacturers who use z-filter approaches do not provide completely free selection of the spiral pitch, but recommend a selection of fixed pitch values aimed at optimizing the z-sampling scheme and reducing spiral artifacts, such as pitch 0.625, 0.75, 0.875, 1.125, 1.25, 1.375, and 1.5 for 4-slice scanning (TAGUCHI 1998).

3.3.4

Multi-slice Spiral Reconstruction with Cone-Beam Algorithms

3.3.4.1

Overview of Cone-Beam Reconstruction Algorithms

For CT scanners with 16 and more slices, modified reconstruction approaches accounting for the cone-

beam geometry of the measurement rays have to be considered. All commercially available multi-slice CT systems providing cone-beam reconstruction rely on approximate algorithms. Although these algorithms are theoretically not exact, image artifacts may be controlled for moderate cone-angle and moderate number of simultaneously acquired slices and kept at a level tolerable for medical CT. Some manufacturers extend the Feldkamp algorithm (FELDKAMP 1984, GRASS 2000), an approximate 3D filtered back-projection reconstruction originally introduced for axial scanning, to multi-slice spiral scanning (WANG 1993, SCHALLER 1998, HEIN 2003). Other manufacturers use variations and extensions of nutating slice algorithms (LARSON 1998, TURBELL 1999, PROKSA 2000, KACHELRIESS 2000, BRUDER 2000), which split the 3D reconstruction task into a series of conventional 2D reconstructions on tilted intermediate image planes. Representative examples are the adaptive multiple plane reconstruction (AMPR) (SCHALLER 2001, FLOHR 2003) and the weighted hyperplane reconstruction (WHR) (HSIEH 2001, HSIEH 2003).

3.3.4.2

3D Filtered Back-Projection

An example of a 3D convolution-back-projection reconstruction is the true cone-beam tomography (TCOT) algorithm implemented in some of the newer 16-slice and 32-slice scanners. In this approach, the measurement rays undergo a filter operation (convolution) in the fan-angle direction and are then back-projected into a 3D volume along the lines of measurement, thus accounting for their cone-beam geometry. To reconstruct a pixel i located at the co-ordinates (x_i, y_i) on the image plane of interest (Fig. 3.6), the ray that passes from the X-ray source through the pixel to the detector array is selected for each projection angle (HEIN 2003). The filtered detector values for all ray sums passing through the pixel for all views are summed up and normalized to create the final reconstructed image. However, 3D back-projection is computationally demanding and requires dedicated hardware to achieve acceptable image-reconstruction times.

Recently, it has been shown that the choice of the proper direction along which the data should be fil-

tered is of critical importance for the image quality achieved with 3D filtered back-projection (STIERSTORFER 2004). If the fan-beam projections are filtered along the fan-angle direction β , as proposed in the original Wang algorithm (WANG 1993), severe artifacts appear for larger cone angles. Filtering of the data in the direction of the spiral tangent can markedly improve image quality. A good approximation is filtering of the data in the p-direction after rebinning to parallel geometry.

3.3.4.3

Adaptive Multiple Plane Reconstruction

The AMPR-approach (SCHALLER 2001, FLOHR 2003) is an extension and generalization of advanced single-slice rebinning (ASSR) (LARSON 1998, KACHELRIESS 2000). AMPR allows for free selection of the spiral pitch with optimized dose utilization, which is beneficial for medical applications. With ASSR, a partial scan interval ($\sim 240^\circ$ of scan data) is used for image reconstruction. The image planes are no longer perpendicular to the patient axis; instead, they are tilted to match the spiral path of the focal spot (Fig. 3.18a).

For every view angle in this partial scan interval, the focal spot is positioned in or nearby the image plane, i.e., measurement rays running in or very close to the image plane are available. These conditions need to be fulfilled for a standard 2D reconstruction. In a final z-reformation step, the traditional axial images are calculated by an interpolation between the tilted original image planes. ASSR encounters its limitations when the spiral pitch is reduced to make use of the overlapping spiral acquisition and the resulting dose accumulation. When a range of projection angles much larger than π (in parallel geometry) for an image are used, it becomes impossible to optimally fit the image plane to the spiral path. The AMPR algorithm (SCHALLER 2001, FLOHR 2003) addresses this problem: instead of using all available data for one single image, the data are distributed to several partial images on double-oblique image planes, which are individually adapted to the spiral path and fan out like the pages of a book (Fig. 3.18b). To ensure full use of the dose, both the number of partial images (the number of "pages" in the book) and the length of the data interval per image depend on the spiral pitch (Fig. 3.19a). The final axial (or arbitrarily oriented) images are calculated by a z-

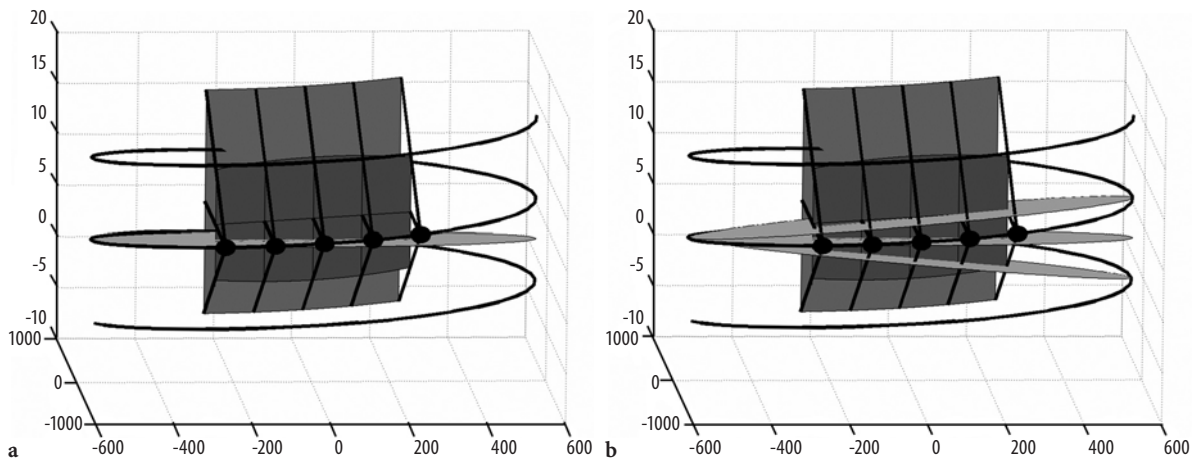


Fig. 3.18. The advanced single-slice rebinning (ASSR) (a) and AMPR (b) approaches. **a** In the ASSR approach, the image plane is attached to the focus at reference projection angle $\theta_r = 0$ (left side). It is tilted by an angle γ around the x-axis. A parallel projection at projection angle $\theta = \pi/2$ is indicated. The dots represent the focus positions for selected rays within this parallel projection. The reconstruction plane optimally fits the spiral path in a projection angle range $[-\pi/2, \pi/2]$. **b** The AMPR approach for a 16 slice detector at pitch = 0.75 using the same perspective as in **a**. Three double-oblique image planes are attached to the focus at reference projection angle $\theta_r = 0$ (left side). The three image planes fan out like the pages of a book. A parallel projection at projection angle $\theta = \pi/2$ is indicated

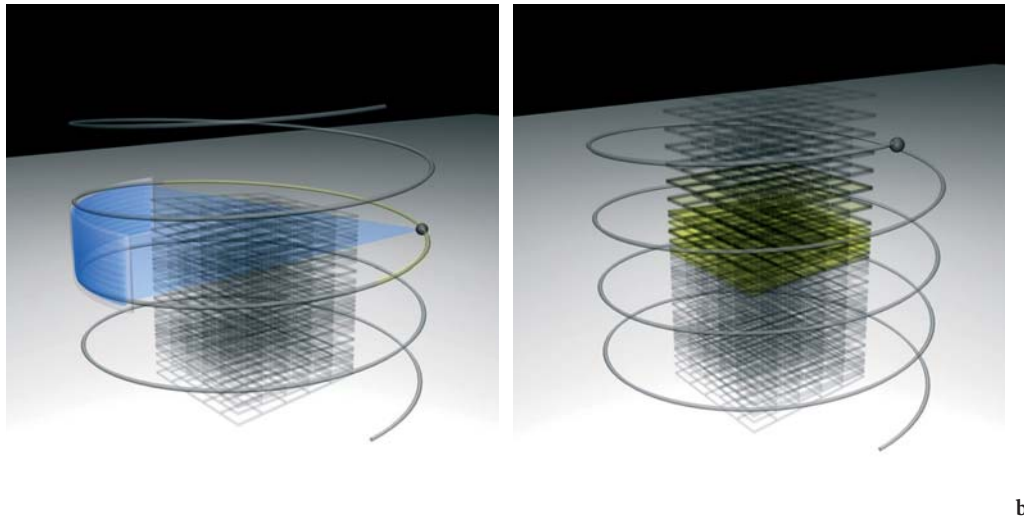


Fig. 3.19a, b. Adaptive multiple plane reconstruction AMPR. **a** Multi-slice spiral data are divided into overlapping pitch-dependent segments. As an intermediate step for each of these segments, partial images are reconstructed on double-oblique image planes that are adapted to the local curvature of the spiral and open like the pages of a book. **b** The resulting images on axial planes are generated via z-reformatting, similar to MPR post-processing

interpolation between the tilted partial image planes (Fig. 3.19b). The shape and the width of the z-interpolation functions are selectable. Different SSPs and different slice widths can therefore be adjusted, so that z-axis resolution (SSP) can be traded off with image noise. The spiral pitch is freely selectable and slice width, and consequently z-axis resolution, are independent of the pitch. The concepts of effective mAs and automatic adaptation of the tube current to the pitch also apply to AMPR.

With the AMPR approach, good image quality is obtained for all pitch values between 0.5 and 1.5 (FLOHR 2002). Figure 3.20 shows an axial slice and a MPR of an anthropomorphic thorax phantom. Scan data for 16×0.75 -mm collimation at pitch 1 was reconstructed with 1-mm slice width, using z-filtering (top), the AMPR algorithm (center), and 3D back-projection (bottom). If the cone-angle is neglected, artifacts are created for high-contrast objects and geometric distortions occur, particularly in MPRs (top). Both AMPR (center) and 3D back-projection (bottom) restore the spatial integrity of high-contrast objects, reduce cone-beam artifacts, and are fully equivalent for 16-slice scanning. Recent studies

have demonstrated the adequacy of extended versions of AMPR for medical CT systems with up to 64 rows (STIERSTORFER 2002). The remaining artifacts shown in Figure 3.20 are spiral interpolation artifacts (“windmill” artifacts), as opposed to cone-beam artifacts. Windmill artifacts are not related to the cone-beam geometry but result from the finite width of the detector rows, which thus requires interpolation between them for image reconstruction. Hence, they occur independently of the reconstruction approach. They are exaggerated in the mathematical phantom shown and can be reduced by either decreasing the pitch and/or increasing the reconstruction slice width relative to the collimation.

Multi-slice spiral scanning using AMPR is characterized by the same key properties as adaptive axial interpolation, as discussed above for z-filter reconstruction. Thus, all recommendations regarding the selection of collimation and pitch that were discussed above also apply for AMPR. In particular, changing the pitch does not change the radiation exposure to the patient, and using higher pitch does not result in dose saving. Narrow collimation scanning should be performed whenever possible.

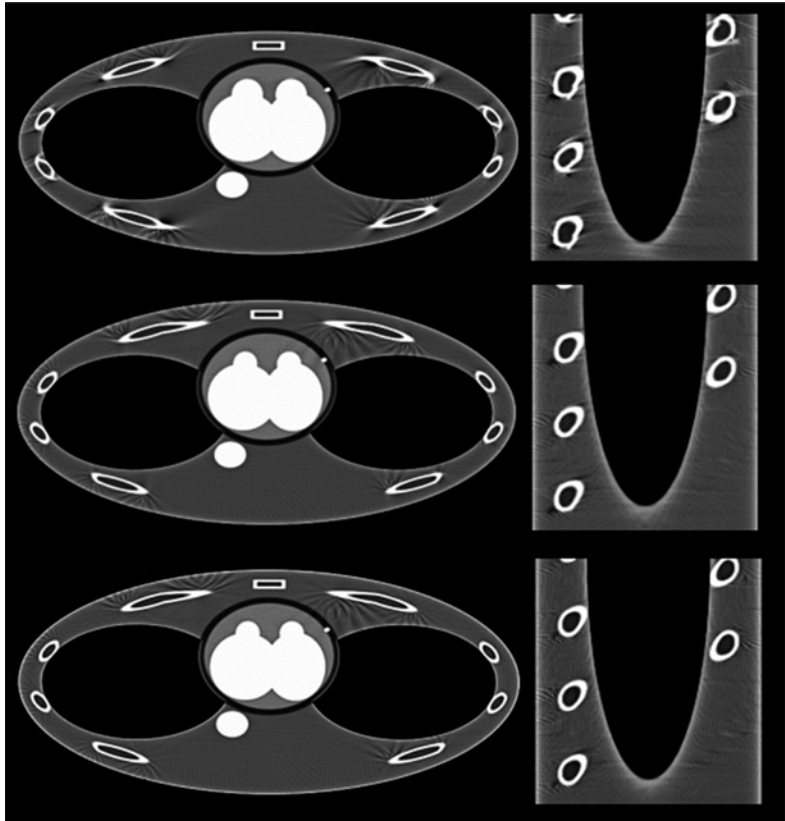


Fig. 3.20. Axial slice and MPR of an anthropomorphic thorax phantom. Scan data for 16×0.75 -mm collimation at pitch 1 was reconstructed with 1-mm slice width and z-filtering, neglecting the cone-angle of the measurement rays (*top*), with the AMPR algorithm (*center*), and with 3D back-projection with optimized filter direction (*bottom*). Neglecting the cone-angle leads to artifacts for high-contrast objects, particularly in MPRs (*top*). Both AMPR (*center*) and 3D back-projection (*bottom*) reduce cone-beam artifacts and are fully equivalent for 16-slice scanning

3.3.4.4 Weighted Hyperplane Reconstruction

The concepts used in WHR, (described in HsIEH 2001, HsIEH 2003) are related to those used in AMPR, yet are derived in a different way. Similar to AMPR, 3D reconstruction is split into a series of 2D reconstructions. Instead of reconstructing traditional axial slices, convex hyper planes are proposed as the region of reconstruction. The increasing spiral overlap with decreasing pitch is handled by introducing subsets of detector rows, which are sufficient

to reconstruct an image at a given pitch value. At pitch = 0.5625 with a 16-slice scanner, the data collected by detector rows 1–9 form a complete projection data set. Similarly, projections from detector rows 2–10 can be used to reconstruct another image at the same z-position; projections from detector rows 3–11 yield a third image, and so on. In a way, these “sub-images” are related to the “book pages” of AMPR. The final image is based on a weighted average of the sub-images. In HsIEH (2003), good image quality for a 16-slice CT system is demonstrated using the WHR approach.

3.3.4.5 Double z-Sampling

In 2004, a new concept for multi-slice spiral scanning was introduced that makes use of a periodic motion of the focal spot in the longitudinal direction to improve data sampling along the z-axis (FLOHR 2004). By permanent electromagnetic deflection of the electron beam in a rotating-envelope X-ray tube (see above), the focal spot is wobbed between two different positions on the anode plate. Due to the anode angle of typically 7–9° this translates into motion both in the radial direction and the z-direction (Fig. 3.21). The radial motion is a side-effect that has to be taken care of by the image-reconstruction algorithms, most favorably in the “rebinning” procedure, which is the interpolation of the measured fan-beam data to parallel geometry. The amplitude of the periodic z-motion is adjusted such that two subsequent readings are shifted by half a collimated slice width in the patient’s longitudinal direction (Fig. 3.22). Therefore, the measurement rays of two subsequent detector read-outs with collimated slice width SW_{coll} interleave in the z-direction, and every two N-slice readings are combined to one 2N-slice projection with a sampling distance of $SW_{\text{coll}}/2$ (Fig. 3.22).

The most recent multi-slice CT system using double z-sampling has a detector that provides 32 collimated 0.6-mm slices. Two subsequent 32-slice

detector read-outs are combined to one 64-slice projection with a sampling distance of 0.3 mm at iso-center. With this technique, 64 overlapping 0.6-mm slices per rotation are acquired. The sampling scheme is identical to that of a 64×0.3 -mm detector, and the AMPR algorithm is used for image reconstruction. In this way, spatial resolution in the longitudinal direction is increased, thus providing a measurable longitudinal spatial resolution of 0.33 mm, and objects below 0.4 mm in diameter can be routinely resolved at any pitch (Fig. 3.23). Another, clinically even more relevant benefit of double z-sampling is the suppression of spiral windmill artifacts at any pitch (Fig. 3.24, 3.25). Double z-sampling provides a sampling distance of $SW_{\text{coll}}/2$ independent of the pitch. The improved sampling along the z-direction is not restricted to the iso-center, but is maintained over a wide range of the SFOV. Longitudinal resolution is therefore not severely degraded for off-center objects. This is a major difference in approaches that attempt to improve longitudinal resolution by the choice of optimized small pitch values, so that data acquired in different rotations interleave in the z-direction. In this case, a sampling distance of $SW_{\text{coll}}/2$ is achieved close to iso-center only.

In conclusion, 16- and 64-slice spiral scanning with cone-beam reconstruction techniques enables scanning of large scan ranges with sub-millimeter resolution and superb image quality. The ability to provide sub-millimeter volume coverage repre-

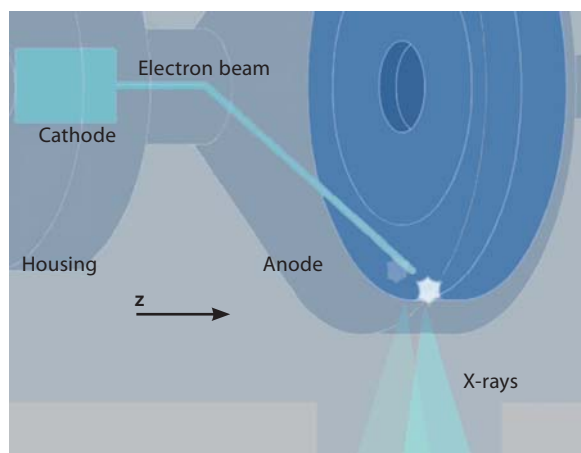


Fig. 3.21. A rotating-envelope X-ray tube (Siemens STRATON, Forchheim, Germany) with z-flying focal spot technique. The entire tube housing rotates in an oil bath. The anode plate is in direct contact with the cooling oil. The central cathode also rotates, and permanent electromagnetic deflection of the electron beam is needed to control the position and the shape of the focal spot. The electromagnetic deflection unit can be used to switch the focal spot between two different positions on the anode plate (indicated by two asterisks). Due to the anode angle of typically 7–9°, this translates into a motion both in the radial direction and the z-direction

sents a significant performance enhancement over 4-slice CT systems. The latest 64-slice CT scanners even allow for coverage of arbitrarily large scan ranges without compromising on spatial resolution. Therefore, 16-slice CT scanners and, even more, 64-slice CT scanners are very well-suited for angiographic applications in all body regions (Figs. 3.26–3.28), which represents one of the most rapidly emerging applications. The use of the latest 16- and 64-slice CT scanners in cardiac applications requires special ECG-gated scan and reconstruction techniques, which will be introduced in the following chapters.

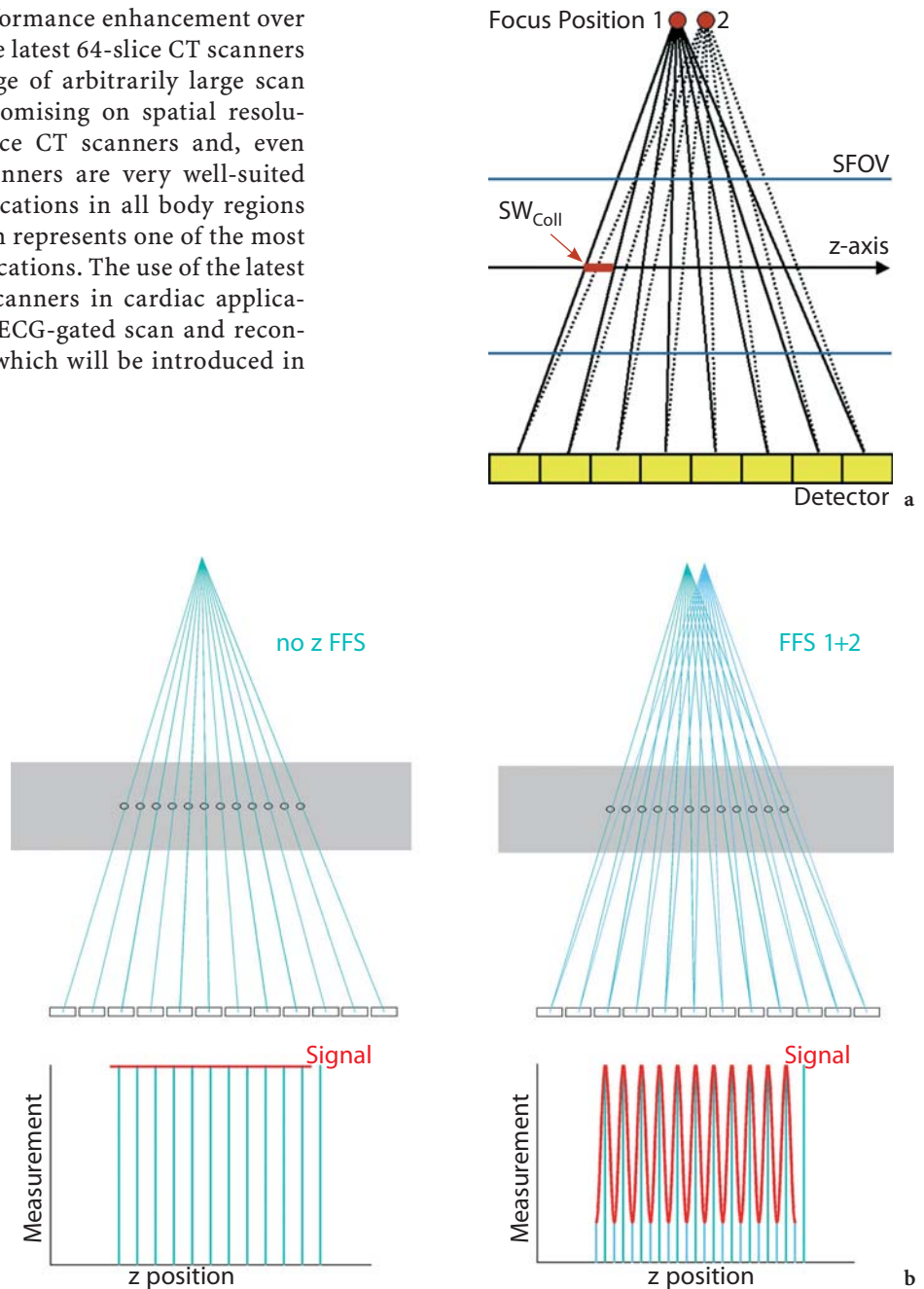


Fig. 3.22a, b. Principle of improved z-sampling with the z-flying focal spot technique. **a** Due to a periodic motion of the focal spot in the z-direction, two subsequent N-slice readings are shifted by half a collimated slice width ($SW_{coll}/2$) at iso-center and can be interleaved to one $2N$ -slice projection. Improved z-sampling is not only achieved at iso-center, but maintained over a wide range of the SFOV. The simultaneous radial motion of the focal spot in an actual X-ray tube has been omitted to simplify the drawing. **b** The improved z-sampling with the z-flying focal spot technique provides consistent resolution of smaller objects due to a finer sampling scheme

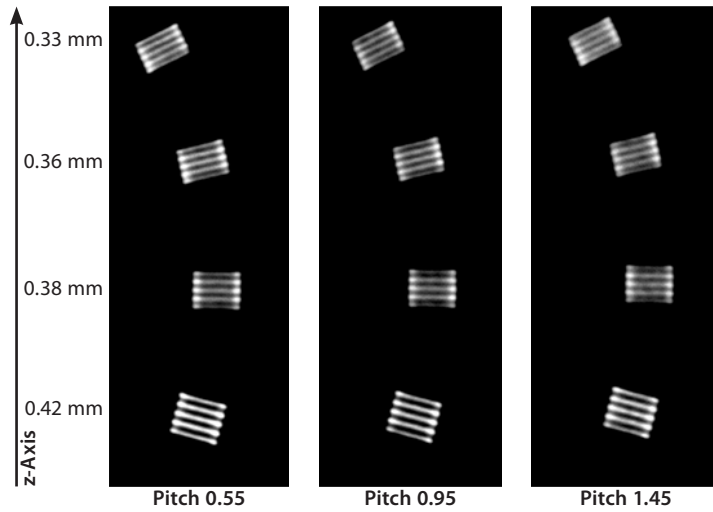


Fig. 3.23. Demonstration of spatial resolution at iso-center for the evaluated 64-slice CT scanner (SOMATOM Sensation 64, Siemens, Forchheim, Germany). The bar patterns of the high-resolution insert of the CATPHAN (computer-assisted tomography phantom, standardized for contrast and resolution measurements) have been aligned in the longitudinal direction (at iso-center). Scan data have been acquired with 64×0.6 -mm slices using the z-flying focal spot and a sharp body reconstruction kernel (B70). Independent of the pitch, the bar patterns down to 0.33 mm bar diameter are visible

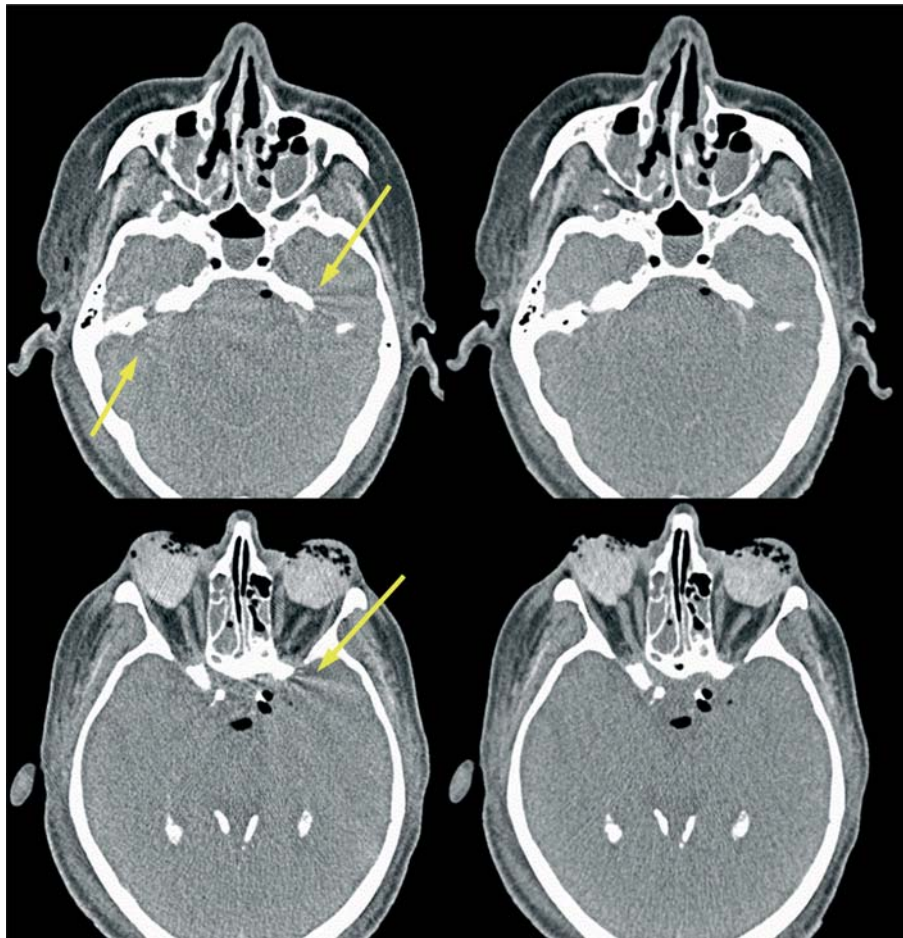


Fig. 3.24. Reduction of spiral artifacts with the z-flying focal spot technique. Left Head specimen scanned with 32×0.6 -mm collimation at pitch 1.4, without z-flying focal spot. Right Head specimen scanned at the same pitch with 64×0.6 -mm slices using the z-flying focal spot technique. Due to the improved longitudinal sampling, spiral interpolation artifacts (the windmill structures indicated by the arrows) are suppressed without degradation of z-axis resolution

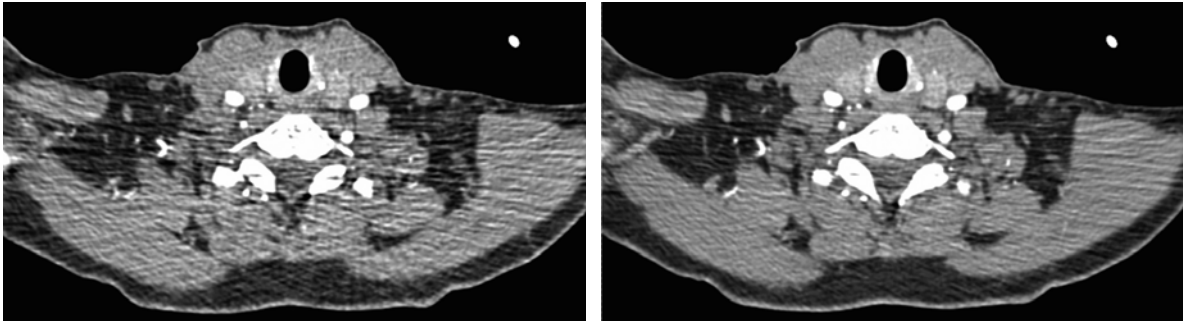


Fig. 3.25. Reduction of spiral artifacts with the z-flying focal spot technique. Left Axial slice at the level of the shoulder scanned with 32×0.6 -mm collimation at pitch 1.4, without z-flying focal spot. Right The same patient and the same z-position scanned with the same pitch with 64×0.6 -mm slices using the z-flying focal spot technique. Due to the improved longitudinal sampling, spiral interpolation artifacts that appear as pronounced streaks propagating from left to right are suppressed without degradation of z-axis resolution

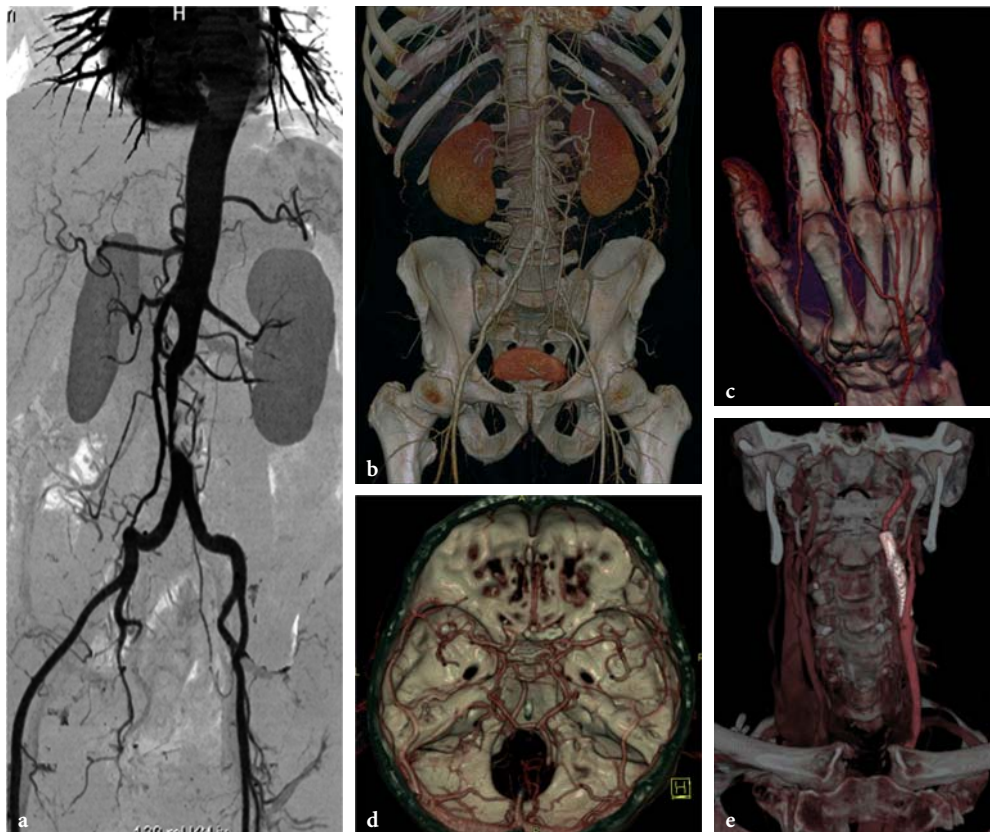


Fig. 3.26a–e. Case examples of 16-slice CT angiography examinations using a CT scanner with 16×0.75 -mm collimation. High-resolution CT angiography of the aorta and iliac arteries with a 1200-mm scan range, visualized in an angiographic-type maximum intensity projections (MIP) display (a) and volume-rendering technique (b). CT angiography examinations of the digital arteries (c), the carotid arteries with an inserted stent (d), and the cerebral vessels (e). (Case courtesy of a, b the University of Tübingen, Germany, and c–e the University of Munich, Grosshadern Clinic, Germany)

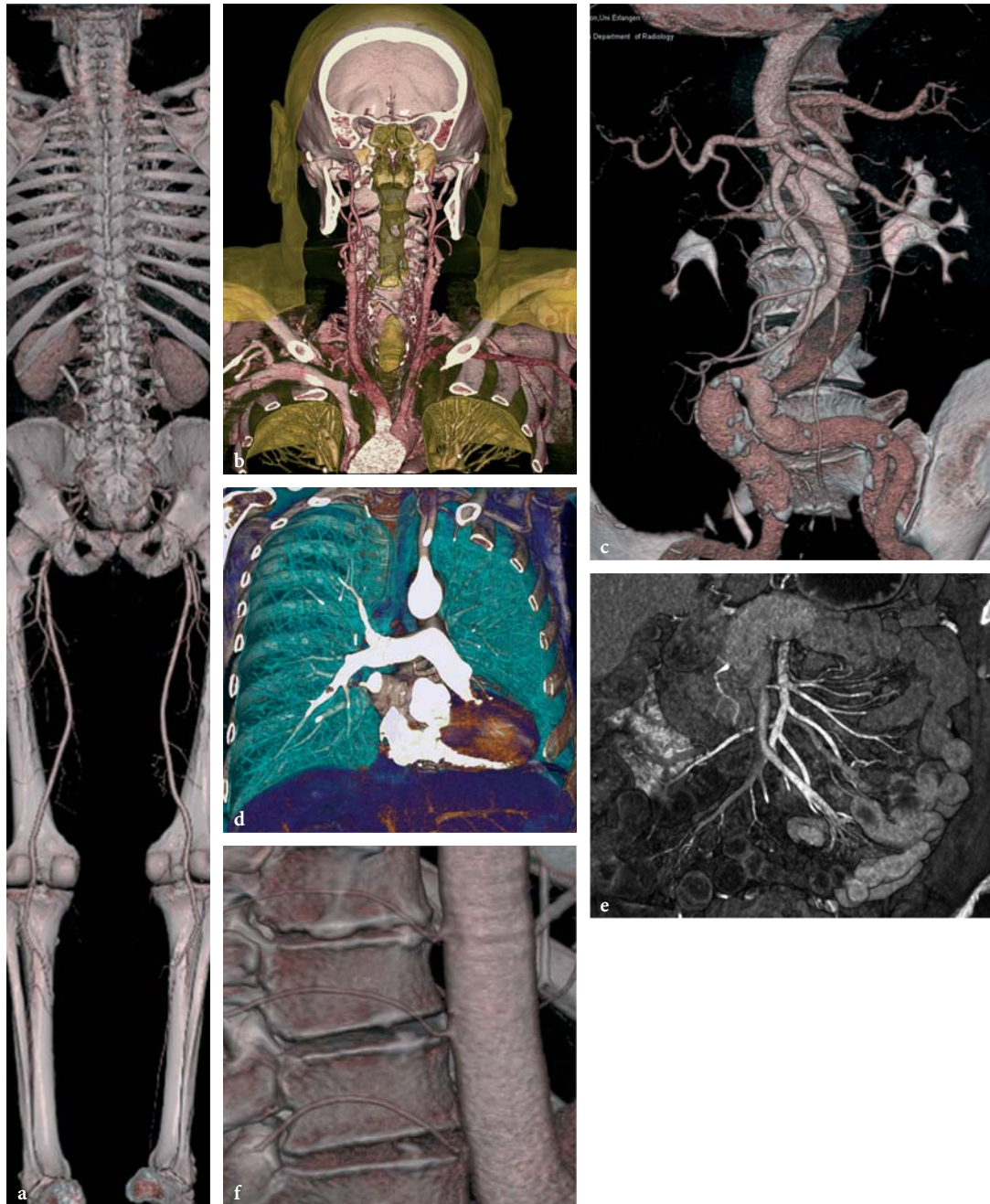


Fig. 3.27a–f. Case examples of 64-slice CT angiography examinations using a CT scanner with 0.6-mm collimation and double z-sampling technique. Whole-body CT angiography examination with 0.4-mm resolution and 1570-mm scan range (a). Pure arterial-phase carotid artery examination in 5-s scan time (b). CT angiography of a dissection of the abdominal aorta with excellent visualization of calcifications and small-caliber abdominal vessels (c). Detection of pulmonary embolism in a patient with chest pain within a breath-hold time of 5 s (d). CT angiography of the mesenteric arteries in a patient with acute bowel ischemia (e). Display of small vessels with calibers of < 1 mm originating from the thoracic aorta perpendicular to the scan axis (f). (Cases courtesy of the University of Erlangen, Germany)

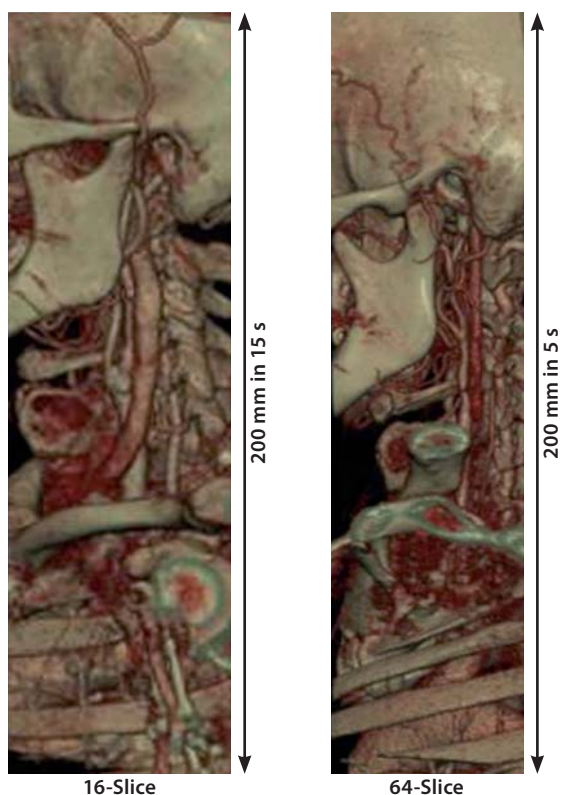


Fig. 3.28. Direct comparison of a CT angiography of the carotid arteries in the same patient, performed with a 16-slice CT at 0.75-mm collimation and with a 64-slice CT using 0.6-mm collimation and double z-sampling technique. Image quality can be greatly improved using 64-slice CT and with significantly shorter scan times due to the absence of strong venous overlap. (Case courtesy of the University of Munich, Grosshadern Clinic, Germany)

References

Achenbach S, Ulzheimer S, Baum U et al (2000). Noninvasive coronary angiography by retrospectively ECG-gated multislice spiral CT. *Circulation* 102:2823–2828

Becker C, Knez A, Ohnesorge B, Schöpf U, Reiser MF (2000). Imaging of non-calcified coronary plaques using helical CT with retrospective EKG gating. *AJR* 175:423–424

Bruder H, Kachelrieß M, Schaller S, Stierstorfer K, Flohr T (2000). Single-slice rebinning reconstruction in spiral cone-beam computed tomography. *IEEE Trans Med Imag* 19(9): 873–887

Crawford CR, King KF (1990). Computed tomography scanning with simultaneous patient translation. *Med Phys* 17: 967–982

Ertl-Wagner B, Hoffmann RT, Brüning R, Dichgans M, Reiser MF (2002). Supraaortale Gefäßdiagnostik mit dem 16-Zeilen-Multidetektor-Spiral-CT. *Untersuchungsprotokoll und erste Erfahrungen. Radiologie* 42:728–732

Feldkamp LA, Davis LC, and Kress JW (1984). Practical cone-beam algorithm. *J Opt Soc Am A* 1 612–619

Flohr T, Stierstorfer K, Bruder H, Simon J, Schaller S (2002a). New Technical developments in multislice CT. Part 1: Approaching isotropic resolution with sub-mm 16-slice Scanning, *Röfo Fortschr Geb Rontgenstr Neuen Bildgeb Verfahr.* 174:839–845

Flohr T, Bruder H, Stierstorfer K, Simon J, Schaller S, Ohnesorge B (2002b). New technical developments in multislice CT. Part 2: Sub-millimeter 16-slice scanning and increased gantry rotation speed for cardiac imaging. *Röfo Fortschr Geb Rontgenstr Neuen bildgeb verfahr* 174:1022–1027

Flohr T, Stierstorfer K, Bruder H, Simon J, Polacin A, Schaller S (2003a). Image reconstruction and image quality evaluation for a 16-slice CT scanner. *Med Phys* 30 (5): 832–845

Flohr T, Ohnesorge B, Bruder H, Stierstorfer K, Simon J, Suess C, Schaller S (2003b). Image reconstruction and performance evaluation for ECG-gated spiral scanning with a 16-slice CT system. *Med Phys* 30(10): 2650–2662

Flohr T, Bruder H, Stierstorfer K, Schaller S (2003c). Evaluation of approaches to reduce spiral artifacts in multi-slice spiral CT (abstract). Abstracts of the 89th scientific assembly and annual meeting of the RSNA 2003, 567

Flohr T, Stierstorfer K, Raupach R, Ulzheimer S, Bruder H (2004). Performance evaluation of a 64-slice CT-system with z-flying focal spot. *Röfo Fortschr Geb Rontgenstr Neuen Bildgeb Verfahr* 176:1803–1810

Fuchs T, Krause J, Schaller S, Flohr T, Kalender WA (2000). Spiral interpolation algorithms for multislice spiral CT. Part 2. Measurement and evaluation of slice sensitivity profiles and noise at a clinical multislice system. *IEEE Trans Med Imag* 19(9): 835–847

Grass M, Köhler T, Proksa R (2000). 3D cone-beam CT reconstruction for circular trajectories. *Phys Med Biol* 45(2):329–347

Hein I, Taguchi K, Silver MD, Kazarna M, Mori I (2003). Feldkamp-based cone-beam reconstruction for gantry-tilted helical multi-slice CT. *Med Phys* 30(12), 3233–3242

Hong C, Becker C R, Huber A, Schoepf U J, Ohnesorge B, Knez A, Brüning R, Reiser MF (2001). ECG-gated reconstructed multi-detector row CT coronary angiography: effect of varying trigger delay on image quality. *Radiology* 220: 712–717

Hu H (1999). Multi-slice helical CT: Scan and reconstruction. *Med Phys* 26(1):5–18

Hu H, He HD, Foley WD, Fox SH (2000). Four multidetector-row helical CT: image quality and volume coverage speed. *Radiology* 215: 55–62

Hsieh J (2001a). Investigation of the slice sensitivity profile for step-and-shoot mode multi-slice computed tomography. *Med Phys* 28: 491–500

Hsieh J, Toth TL, Simoni P, Grekovicz B, Slack CC, Seidenschner GE (2001b). A generalized helical reconstruction

- algorithm for multi-slice CT. Abstracts of the 87th Scientific Assembly and Annual Meeting of the RSNA 2001 271
- Hsieh J (2003a). Analytical models for multi-slice helical CT performance parameters. *Med Phys* 30(2): 169–178
- Hsieh J, Grekowitz B, Simoni P, Thibault JB, Joshi MC, Dutta S, Williams EC, Shaughnessy C, Sainath P (2003b). Convolution reconstruction algorithm for multi-slice helical CT. In: *Proc. SPIE Int Symp Med Imag* 2003
- Kachelrieß M, Schaller S, Kalender WA (2000a). Advanced single-slice rebinning in cone-beam spiral CT. *Med Phys* 27: 754–772
- Kachelrieß M, Ulzheimer S, Kalender W (2000b). ECG-correlated image reconstruction from subsecond multi-slice spiral CT scans of the heart. *Med Phys* 27: 1881–1902
- Kalender W, Seissler W, Klotz E, Vock P (1990). Spiral volumetric CT with single-breath-hold technique, continuous transport and continuous scanner rotation. *Radiology* 176: 181–183
- Kalender W (1995). Thin-section three-dimensional spiral CT: is isotropic imaging possible? *Radiology* 197: 578–580
- Klingenberg-Regn K, Schaller S, Flohr T, Ohnesorge B, Kopp AF, Baum U (1999). Subsecond multi-slice computed tomography: basics and applications. *EJR* 31:110–124
- Knez A, Becker C, Leber A, Ohnesorge B, Reiser MF, Haberl R (2000). Non-invasive assessment of coronary artery stenoses with multidetector helical computed tomography. *Circulation* 101: e221-e222
- Kopp A, Schröder S, Küttner A et al (2001). Coronary arteries: retrospectively ecg-gated multidetector row CT angiography with selective optimization of the image reconstruction window. *Radiology* 221: 683–688
- Larson G, Ruth C, Crawford C (1998). Nutating slice CT image reconstruction. US Patent Application WO 98/44847, filed 8 April, 1998
- Lell M, Wildberger J, Heuschmid M, Flohr T, Stierstorfer K, Fellner F, Lang W, Bautz W, Baum U (2002). CT-Angiographie der A. carotis: Erste Erfahrungen mit einem 16-Schicht-Spiral-CT – CT-angiography of the carotid artery: First results with a novel 16-slice-spiral-CT scanner, *Röfo Fortschr Geb Rontgenstr Neuen Bildgeb Verfahr* 174: 1165–1169
- Liang Y, Kruger RA (1996). Dual-slice spiral versus single-slice spiral scanning: comparison of the physical performance of two computed tomography scanners. *Med Phys* 23(2): 205–220
- Macari, M, Bini MJ, Xue X, et al (2002). Colorectal neoplasms: prospective comparison of thin-section low-dose multi-detector row CT colonography and conventional colonoscopy for detection. *Radiology* 224:383–392
- McCullough CH, Zink FE (1999). Performance evaluation of a multi-slice CT system. *Med Phys* 26:2223–2230
- Nieman K, Oudkerk M, Rensing B, van Oijen P, Munne A, van Geuns R, de Feyter P (2001). Coronary angiography with multi-slice coputed tomography. *The Lancet* 357: 599–603
- Nieman K, Cademartiri F, Lemos PA, Raaijmakers R, Pattynama PMT, de Feyter PJ (2002). Reliable noninvasive coronary angiography with fast submillimeter multislice spiral computed tomography. *Circulation* 106: 2051–2054
- Ohnesorge B, Flohr T, Schaller S, Klingenberg-Regn K, Becker C, Schöpf U J, Brüning R, Reiser MF (1999). Technische Grundlagen und Anwendungen der Mehrschicht-CT (German). *Radiologe* 39:923–931
- Ohnesorge B, Flohr T, Becker C, Kopp A, Schoepf U, Baum U, Knez A, Klingenberg-Regn K, Reiser MF (2000). Cardiac imaging by means of electro-cardiographically gated multisection spiral CT – initial experience. *Radiology* 217:564–571
- Ohnesorge B, Kopp AF, Becker CR, Knez A, Schröder S, Flohr T (2001). Technical aspects of cardiovascular and cardiac diagnosis with CT. In: *Topol E and Lanzer P, Theory and practise of cardiovascular medicine II. Chap. 15:121–130. Springer Verlag Berlin, Heidelberg*
- Proksa R, Koehler T, Grass M, Timmer J (2000). The n-PI Method for helical cone-beam CT. *IEEE Trans Med Imag* 19:848 – 863
- Remy-Jardin J, Tillie-Leblond I, Szapiro D et al (2002). CT angiography of pulmonary embolism in patents with underlying respiratory disease: impact of multi-slice CT on image quality and negative predictive value. *Eur Radiol* 12: 1971–1978
- Ropers D, Baum U, Pohle K, et al (2003). Detection of coronary artery stenoses with thin-slice multi-detector row spiral computed tomography and multiplanar reconstruction. *Circulation* 107:664–6
- Rubin GD, Dake MD, Semba CP (1995). Current status of three-dimensional spiral CT scanning for imaging the vasculature. *Radiol Clin North Am* 33(1): 51–70 (Review)
- Rubin GD, Schmidt AJ, Logan LJ, Sofilos MC (2001). Multi-detector row CT angiography of lower extremity arterial inflow and runoff: initial experience. *Radiology* 221(1): 146–58
- Saito Y, Suzuki T (1998). Evaluation of the performance of multi-slice CT system in non-helical scanning, Abstracts of the 84th Scientific Assembly and Annual Meeting of the RSNA 1998, 578
- Schaller S (1998). Practical image reconstruction for cone-beam computed tomography, PhD-Thesis University Erlangen Nürnberg, Germany
- Schaller S, Flohr T, Klingenberg K, Krause J, Fuchs T, Kalender WA (2000). Spiral interpolation algorithm for multi-slice spiral CT. Part I: Theory. *IEEE Trans Med Imag* 19(9): 822–834
- Schaller S, Stierstorfer K, Bruder H, Kachelrieß M, Flohr T (2001). Novel approximate approach for high-quality image reconstruction in helical cone beam CT at arbitrary pitch. In: *Proc SPIE Int Symp Med Imag* 4322:113–127
- Schardt P, Kutschera W, Knüpfer W (2004). Technical design and performance evaluation of a new rotation envelope tube concept in X-ray computed tomography. *Med Phys* 31:2699–2706
- Schöpf U J, Bruening R D, Hong C, Eibel R, Aydemir S, Crispin A, Becker C, Reiser MF (2001). Multislice helical CT of focal and diffuse lung disease: comprehensive diagnosis with reconstruction of contiguous and high-resolution CT sections from a single thin-collimation scan. *AJR Am J Roentgenol* 177(1):179–84

- Schoepf UJ, Becker CR, Hofmann LK, Das M, Flohr T, Ohnesorge BM (2003). Multislice CT angiography. *Eur Radiol* 13:1946–1961
- Schroeder S, Kopp A, Baumbach A, Meisner C, Kuettner A, Georg C, Ohnesorge B, Herdeg C, Claussen C, Karsch K (2001a). Noninvasive detection and evaluation of atherosclerotic coronary plaques with multi-slice computed tomography. *JACC* 37(5): 1430–1435
- Schroeder S, Flohr T, Kopp A F, Meisner C, Kuettner A, Herdeg C, Baumbach A, Ohnesorge B (2001b). Accuracy of density measurements within plaques located in artificial coronary arteries by X-Ray multislice CT: results of a phantom study. *JCAT* 25(6): 900–906
- Stierstorfer K, Flohr T, Bruder H (2002). Segmented multiple plane reconstruction- a novel approximate reconstruction scheme for multi-slice spiral CT. *Phys Med Biol* 47:2571–2581
- Stierstorfer K, Rauscher R, Boese J, Bruder H, Schaller S, Flohr T (2004). Weighted FBP- a simple approximate 3D FBP algorithm for multi-slice spiral CT with good dose usage for arbitrary pitch. *Phys Med Biol* 49:2209–2218
- Swensen SJ (2002). CT screening for lung cancer. *AJR* 179:833–836
- Taguchi T, Aradate H (1998). Algorithm for image reconstruction in multi-slice helical CT. *Med Phys* 25(4): 550–561
- Tomandl BF, Klotz E, Handschu R, Stemper B, Reinhardt F, Huk WJ, Eberhardt KE, Fateh-Moghadem S (2003). Comprehensive imaging of ischemic stroke with multisection CT. *RadioGraphics* 23(3):565–592
- Turbell H, Danielsson PE (1999). An improved PI-method for reconstruction from helical cone beam projections. In: *IEEE Medical Imaging Conference*, Seattle
- Villablanca J P, Lahan R, Hooshi P, Lim S, Duckwiler G, Patel A, Sayre J, Martin N, Frazee J, Bentson J, Vinuela F (2002). Detection and characterization of very small cerebral aneurysms by using 2D and 3D helical CT angiography. *AJNR Am J Neuroradiol* 23(7):1187–98
- Wang G, Lin T, Cheng P (1993). A general cone-beam reconstruction algorithm. *IEEE Trans Med Imag* 12, 486–496
- Wessling J, Fischbach R, Meier N, et al (2003). CT colonography: protocol optimization with multi-detector row CT – study in an anthropomorphic colon phantom. *Radiology* 228:753–759
- Wintersperger B, Helmberger T, Herzog P, Jakobs T, Wagger-shauser T, Becker C, Reiser MF (2002a). Hochoaufgelöste abdominelle Übersichtsangiographie mit einem 16-Detektorzeilen-CT-System – New abdominal CT angiography protocol on a 16 detector-row CT scanner. *Radiologe* 42: 722–727
- Wintersperger B, Herzog P, Jakobs T, Reiser MF, Becker C. Initial experience with the clinical use of a 16 detector row CT system (2002b). *Crit Rev Comput Tomogr* 43:283–316